J. Fluid Mech. (2021), *vol*. 922, A24, doi:10.1017/jfm.2021.524

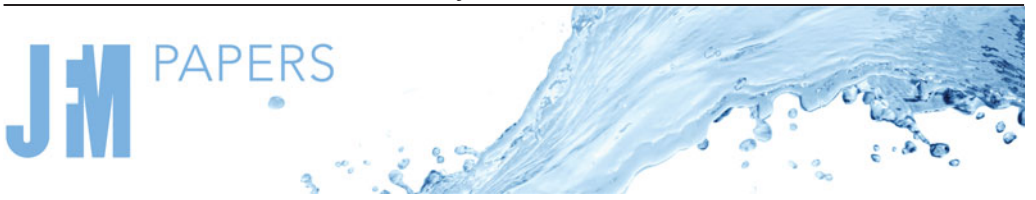

Investigation of high-pressure turbulent jets using direct numerical simulation

Nek Sharan[1,‡] **and Josette Bellan**[1,2,†]

[1]Department of Mechanical and Civil Engineering, California Institute of Technology, Pasadena, CA 91125, USA

[2]Jet Propulsion Laboratory, California Institute of Technology, Pasadena, CA 91109, USA

(Received 16 September 2020; revised 6 April 2021; accepted 7 June 2021)

Direct numerical simulations of free round jets at a Reynolds number (Re_D) of 5000, based on jet diameter (D) and jet-exit bulk velocity (U_e), are performed to study jet turbulence characteristics at supercritical pressures. The jet consists of nitrogen (N_2) that is injected into N_2 at the same temperature. To understand turbulent mixing, a passive scalar is transported with the flow at unity Schmidt number. Two sets of inflow conditions that model jets issuing from either a smooth contraction nozzle (laminar inflow) or a long pipe nozzle (turbulent inflow) are considered. By changing one parameter at a time, the simulations examine the jet-flow sensitivity to the thermodynamic condition (characterized in terms of the compressibility factor (Z) and the normalized isothermal compressibility), inflow condition and ambient pressure (p_∞) spanning perfect- to real-gas conditions. The inflow affects flow statistics in the near field (containing the potential core closure and the transition region) as well as further downstream (containing fully developed flow with self-similar statistics) at both atmospheric and supercritical p_∞. The sensitivity to inflow is larger in the transition region, where the laminar-inflow jets exhibit dominant coherent structures that produce higher mean strain rates and higher turbulent kinetic energy than in turbulent-inflow jets. Decreasing Z at a fixed supercritical p_∞ enhances pressure and density fluctuations (non-dimensionalized by local mean pressure and density, respectively), but the effect on velocity fluctuations depends also on the local flow dynamics. When Z is reduced, large mean strain rates in the transition region of laminar-inflow jets significantly enhance velocity fluctuations (non-dimensionalized by local mean velocity) and scalar mixing, whereas the effects are minimal in jets from turbulent inflow.

Key words: general fluid mechanics, turbulent mixing

† Email address for correspondence: josette.bellan@jpl.nasa.gov
‡ Present address: CCS-2, Los Alamos National Laboratory, Los Alamos, NM 87544, USA.

1. Introduction

Fuel injection and turbulent mixing in numerous applications, e.g. diesel, gas turbine and liquid-rocket engines, occur at pressures and temperatures that may exceed the critical values of injected fuel and oxidizer. At such high pressure (high p), species properties are significantly different from those at atmospheric p. Flow development, mixed-fluid composition and thermal field evolution under supercritical p is characterized by strong nonlinear coupling among the dynamics, transport properties and thermodynamics (e.g. Okong'o & Bellan 2002*b*; Okong'o, Harstad & Bellan 2002; Masi *et al.* 2013) that influences power generation, soot formation and thermal efficiency of the engines.

The current state-of-the-art in modelling such flows is considerably more advanced than the experimental diagnostics that may produce reliable data for model evaluation under such conditions. Indeed, high-order turbulence statistics at engine-relevant high-p conditions are difficult to measure and, as of now, remain unavailable. Table 1 lists a sample of supercritical round-jet experimental studies and the flow conditions considered in those experiments. All studies provide only a qualitative assessment of the jet-flow turbulence, highlighting the challenge of obtaining high-fidelity measurements under these conditions. Additionally, several input parameters necessary to perform corresponding numerical simulations are not always reported. Accurate simulations not only require a careful choice of equation of state, multi-species mass and thermal diffusion models and, at high Reynolds numbers, subgrid-scale models, but also a matching inflow and boundary conditions to the experiment that are not always available. A large-Reynolds-number (Re_D) multi-species simulation involves several models, a fact which complicates isolation of individual model errors and a reliable study of jet turbulence characteristics. Moreover, jet turbulence and its sensitivity to flow parameters at supercritical conditions are not well understood even in a simple single-species setting. Indeed, previous high-p studies mostly examined temporal shear-layer configurations (e.g. Okong'o & Bellan 2002*b*; Okong'o *et al.* 2002; Masi *et al.* 2013; Sciacovelli & Bellan 2019). A few studies of spatially evolving turbulent jets (e.g. Gnanaskandan & Bellan 2017, 2018) have focused on large-eddy simulation (LES) modelling and on direct numerical simulation (DNS) of binary-species diffusion, but did not address the influence of ambient pressure and thermodynamic departure from perfect gas on jet turbulence. The present study fills that void by performing DNSs of single-species round jets at various ambient (chamber) pressures (p_∞), compressibility factors (Z) and inflow conditions.

Effects of (dynamics-based) compressibility, defined in terms of various (convective, turbulence, gradient, deformation) Mach numbers, on free-shear flows have been investigated at perfect-gas conditions in numerous studies, e.g. Papamoschou & Roshko (1988), Lele (1994), Vreman, Sandham & Luo (1996), Freund, Lele & Moin (2000) and Pantano & Sarkar (2002). In general, an increase in this compressibility, referred to here as dynamic compressibility, is associated with reduced turbulence kinetic energy (t.k.e.) and reduced momentum-thickness growth rate in shear layers. The reduction is attributed to a decrease in t.k.e. production resulting from reduced pressure fluctuations in the pressure-strain term (Vreman *et al.* 1996). For homogeneous shear flow, the rapid-distortion-theory results of Simone, Coleman & Cambon (1997) showed that the t.k.e. change with dynamic compressibility depends on a non-dimensional time based on the mean strain rate. These studies also found that dynamic compressibility influences t.k.e. largely by altering the 'structure' of turbulence and less so by the dilatational terms in the t.k.e. equation. Real-gas effects at high pressure introduce a different type

https://doi.org/10.1017/jfm.2021.524 Published online by Cambridge University Press

Reference	Species (injected + chamber)	U_e (m s)$^{-1}$	$T_{r,ch}$	$T_{r,inj}$	$p_{r,ch}$	$p_{r,inj}$	$Re_D \times 10^3$ ($\rho_e U_e D/\mu$)
Newman & Brzustowski (1971)	$LCO_2 + CO_2/N_2$	2.0–4.0	0.97–1.09	0.97	0.86–1.23	N/A	∼20–30
Woodward & Talley (1996)	$LN_2 + N_2$/He	∼1.8–2.2	2.21–2.46	0.70–0.91	0.83–2.03	N/A	3.4–4.1
Mayer *et al.* (1998)	$LN_2 + N_2$	1	2.38	0.83	0.59–1.18	N/A	∼18–19
		1.3	1.98	0.71	0.83–2.03	N/A	∼21–23
	LN_2 + He	1.7	**2.31**	0.66	**1.62–2.44**	N/A	∼23–24
Oschwald & Schik (1999)	$LN_2 + N_2$	5.0–20.0	2.36	0.79–1.11	1.17–1.76	N/A	115–340
Chehroudi, Talley & Coy (2002)	$LN_2 + N_2$	10.0–15.0	2.38	0.71–0.87	0.23–2.74	N/A	25–75
Mayer *et al.* (2003)	$LN_2 + N_2$	1.8–5.4	2.36	1.0–1.11	3.95–5.98	N/A	∼47–157
Segal & Polikhov (2008)	Fluoroketone + N_2	7.0–25.0	**0.66–1.07**	0.68–1.28	**0.05–1.86**	0.2–2.2	11–42
Roy, Joly & Segal (2013)	Fluoroketone + N_2	7.07–30.0	**0.69–1.09**	1.0–1.31	**1.26–1.88**	1.34–1.98	N/A
Falgout *et al.* (2015)	Dodecane + Air	N/A	**0.7 & 1.4**	0.55	**1.6 & 3.2**	82.55	N/A
Muthukumaran & Vaidyanathan (2016*a*,*b*)	Fluoroketone + N_2	0.86–7.5	**0.82–1.03**	0.99–1.07	**0.81–1.34**	N/A	N/A
	Fluoroketone + He	0.82–19.0	**0.82–1.05**	0.98–1.07	**0.72–1.34**	N/A	N/A
Baab *et al.* (2016, 2018)	n-hexane + N_2	∼91	**0.58**	1.24	**1.65**	1.81	120
	n-pentane + N_2	76 & 96	**0.63**	1.28 & 1.13	**1.48**	1.62 & 1.61	121–139
	Fluoroketone + N_2	41 & 72	**0.67**	1.13	**1.34 & 2.11**	2.11	172–272
Poursadegh *et al.* (2017)	Propane + N_2	N/A	**0.9–1.35**	0.9–0.93	**0.7–1.18**	4.7	N/A
	Propane + N_2	N/A	**1.35**	1.06	**1.3**	4.7	N/A
Gao *et al.* (2019)	RP-3 kerosene + Air	N/A	**0.45**	0.96–1.17	**0.042**	0.84–1.88	N/A
	N_2 + Air	∼254.8–2374.2	**2.28**	4.91–6.02	**0.029**	0.59–1.32	∼87.7–341

Table 1. High-pressure round-jet experimental studies; U_e = jet-exit bulk velocity, $T_{r,ch}$ = chamber reduced temperature, $T_{r,inj}$ = injectant reduced temperature, $p_{r,ch}$ = chamber reduced pressure, $p_{r,inj}$ = injectant reduced pressure, ρ_e = jet-exit (or injectant) fluid density, N/A = not available; ∼ denotes values not provided in the reference but deduced from other parameters. Numbers in bold denote reduced chamber conditions based on injectant critical temperature and pressure.

of compressibility, a thermodynamics-based compressibility characterized by

$$Z \equiv \frac{p}{(\rho R_u T/m)}, \tag{1.1}$$

where ρ is the density, T denotes the temperature, R_u is the universal gas constant and m is the species molar mass. Unlike non-dimensional parameters in fluid dynamics, such as the Reynolds, Prandtl and Schmidt numbers, which measure the relative importance of two different physical phenomena, Z measures the physical effects of intermolecular forces and finite volume of gas molecules. In this study, using Z as one of the important non-dimensional thermodynamic parameters, the effects of thermodynamic compressibility on jet-spread rate and t.k.e. production are examined to determine the physical mechanism by which changes in Z influence jet-flow turbulence.

Turbulent free-shear flow computations are sensitive to the choices of initial/inflow conditions, domain size and numerical discretization (Balaras, Piomelli & Wallace 2001; Mattner 2011; Sharan, Matheou & Dimotakis 2018*a*). In particular, several experimental (e.g. Wygnanski, Champagne & Marasli 1986; Slessor, Bond & Dimotakis 1998; Mi, Nobes & Nathan 2001) and computational (e.g. Ghosal & Rogers 1997; Boersma, Brethouwer & Nieuwstadt 1998; Grinstein 2001) studies have observed near- as well as far-field flow sensitivity to inflow conditions, supporting the theoretical arguments of George (1989) on the existence of various self-similar states determined by the initial/inflow condition. Experimental jet-flow studies typically use a smooth contraction nozzle or a long straight pipe to initialize jet flows (Mi *et al.* 2001). The smooth contraction nozzle produces a laminar inflow with 'top-hat' velocity profile, whereas the long straight pipe produces a fully developed turbulent inflow. Both inflow cases are studied here, first, to examine the sensitivity of presumably existing self-similar states to thermodynamic conditions and, second, to determine how the effects of p_∞ and Z are influenced by inflow change. While it is well known that perfect-gas jets attain a self-similar state, the equivalent information for compressible real-gas jets is unclear. Additionally, conclusions from the studies of inflow effects on incompressible jets (e.g. Boersma *et al.* 1998) need not necessarily extend to compressible jets, and therefore, the inflow effects on compressible real-gas jets are explored in this study.

The present study addresses both perfect-gas jet flows, for which theoretical (e.g. Morris 1983; Michalke 1984) and experimental (e.g. Wygnanski & Fiedler 1969; Panchapakesan & Lumley 1993; Hussein, Capp & George 1994) results exist, and high-p supercritical jets, for which detailed turbulence statistics similar to those of perfect-gas jets do not exist, as discussed above. Accurate high-p numerical simulations that correctly account for the nonlinear coupling of thermodynamic variables with mass and thermal diffusion are challenging. Masi *et al.* (2013) used a multi-species model (previously proposed by Okong'o & Bellan 2002*b*) to account for these nonlinear effects and used the model for DNS of temporal mixing layers. The present study applies that model to single-species spatially developing jet flows, as a precursor to multi-species jet simulations. The results from this study provide a database to compare and contrast turbulence statistics from anticipated high-p multi-species jet calculations and to initiate studies to validate LES models for supercritical flows (e.g. Schmitt *et al.* 2010; Selle & Schmitt 2010; Taşkinoğlu & Bellan 2010, 2011). A recent single-species round-jet DNS study (Ries *et al.* 2017) examined turbulence statistics and heat transport in a supercritical cold jet using the low-Mach-number equations that decouple pressure and density calculation to neglect the acoustic and compressibility effects. In contrast, the present study solves the fully compressible equations for jets at a variety of thermodynamic and inflow conditions.

The paper is organized as follows. The governing equations for single-species flow at atmospheric and supercritical p_∞ are discussed in § 2. The numerical discretization and computational set-up are described in § 3.1. Details of the boundary conditions and the two inflow conditions considered in this study are provided in § 3.2. The results are presented and discussed in § 4: § 4.1 provides an assessment of the effects of p_∞ and Z at a fixed supercritical p_∞ and jet-exit (inflow) bulk velocity U_e; the influence of p_∞ at a fixed Z is examined in § 4.2; the effects of p_∞ and Z at a fixed jet-exit (inflow) Mach number Ma_e, to distinguish them from the cases with a fixed U_e, is investigated in § 4.3; § 4.4 evaluates the effects of inflow change at atmospheric and supercritical p_∞. A discussion of the observed results and conclusions is provided in § 5. In addition, a validation of the equation of state and the transport coefficient models used in this study at high pressures is presented in Appendix A, a grid convergence study is described in Appendix B and a validation of the perfect-gas simulation results against experimental data is discussed in Appendix C.

2. Flow conditions and governing equations

Table 2 summarizes the thermodynamic conditions for the present numerical simulations. Various flow conditions are considered to examine influences of high-p thermodynamics and inflow conditions on round-jet-flow statistics. All conditions, simply called 'cases', simulate single-species N_2 jets issuing into a quiescent chamber at a Re_D of 5000. In each case, the injected and ambient (chamber) fluid temperature and pressure have the same value, i.e. the jet injects into a chamber fluid that is as dense as the injected fluid. Figure 1(a) shows Z of pure N_2 for a temperature range at $p = 50$ bar and $p = 70$ bar with the ambient thermodynamic state of various high-p cases denoted by markers. Figure 1(b) shows the locations of those cases on the supercritical p–T diagram of N_2 and their proximity to the Widom line (depicted as dashed black line) which emanates from the critical point and divides the supercritical regime into a liquid-like fluid at smaller T_r and a gas-like fluid at larger T_r (Simeoni *et al.* 2010; Banuti, Raju & Ihme 2017). For case 2, at the (p_∞, T_∞) conditions, $Z \approx 0.994$; for case 3, $Z \approx 0.9$; while for case 4, $Z \approx 0.8$, thus, representing significant departure from perfect-gas behaviour. Cases 2 to 4 investigate the effect of Z; case 2 is furthest from the Widom line, whereas case 4 is the closest. Case 5 compared against case 3 examines the influence of p_∞ at constant Z. To further characterize the real-gas effects in various cases, the values of isothermal compressibility, β_T, and isentropic (or adiabatic) compressibility, β_S, for ambient condition in various cases are listed in table 3. The values of β_T and β_S can be obtained as a function of Z using

$$\beta_T = -\frac{1}{V}\left(\frac{\partial V}{\partial p}\right)_T = \frac{1}{p} - \frac{1}{Z}\left(\frac{\partial Z}{\partial p}\right)_T, \tag{2.1}$$

$$\beta_S = -\frac{1}{V}\left(\frac{\partial V}{\partial p}\right)_S = \frac{\beta_T}{\gamma}, \tag{2.2}$$

where V is the volume, γ denotes the ratio of the heat capacity at constant pressure to the heat capacity at constant volume and S denotes the entropy. Here, β_T and β_S are dimensional quantities with units of inverse of pressure, and a direct comparison of their values across various cases turns out not to be very informative. However, for a perfect gas, $\beta_T = 1/p$, and the real-gas effect at ambient conditions may be isolated from β_T by examining $\beta_T - 1/p_\infty$ non-dimensionalized using p_∞. The non-dimensional quantity $p_\infty(\beta_T - 1/p_\infty)$ is listed in table 3 and will be used to explain the pressure/density fluctuations observed among various cases in § 4.

Case (description)	$N_x \times N_y \times N_z$	p_∞ (bar)	$T_{ch}(= T_{inj})$ (K)	Z	$\mathcal{F}$	Ma_e	Inflow perturbation
1 (atm-p)	$240 \times 216 \times 216$ $320 \times 288 \times 288$ $400 \times 320 \times 320$	1	293	1.0	6.5	0.6	$0.004U_e$ (lam)
2 (high-p(50); $Z \approx 1$)	$240 \times 216 \times 216$ $320 \times 288 \times 288$ $400 \times 320 \times 320$ $480 \times 360 \times 360$	50	293	0.99	309.4	0.58	$0.004U_e$ (lam)
3 (high-p(50); $Z \approx 0.9$)	$400 \times 320 \times 320$ $480 \times 360 \times 360$	50	199	0.9	641.4	0.73	$0.004U_e$ (lam)
4 (high-p(50); $Z \approx 0.8$)	$400 \times 320 \times 320$ $480 \times 360 \times 360$ $560 \times 408 \times 408$	50	170	0.8	895.7	0.82	$0.004U_e$ (lam)
5 (high-p(70); $Z \approx 0.9$)	$400 \times 320 \times 320$ $480 \times 360 \times 360$	70	211	0.9	774.1	0.69	$0.004U_e$ (lam)
2M (high-p(50); $Z \approx 1$)	$400 \times 320 \times 320$	50	293	0.99	309.4	0.6	$0.004U_e$ (lam)
4M (high-p(50); $Z \approx 0.8$)	$480 \times 360 \times 360$	50	170	0.8	895.7	0.6	$0.004U_e$ (lam)
1T (atm-p)	$400 \times 320 \times 320$	1	293	1.0	6.5	0.6	pipe-flow turb
2T (high-p(50); $Z \approx 1$)	$400 \times 320 \times 320$	50	293	0.99	309.4	0.58	pipe-flow turb
4T (high-p(50); $Z \approx 0.8$)	$480 \times 360 \times 360$	50	170	0.8	895.7	0.82	pipe-flow turb

Table 2. Summary of the parameters for numerical simulations. The subscripts '*inj*' and '*ch*' denote the injection and chamber conditions, respectively; $p_{ch} \equiv p_\infty$ and $T_{ch} \equiv T_\infty$, 'lam' associated with a inflow perturbation denotes laminar conditions. Suffix 'M' in the name of a case, e.g. 2M and 4M, denotes high-p cases with same Mach number as case 1. Suffix 'T' in the name of a case, e.g. 1T, 2T and 4T, denotes turbulent-inflow cases.

The jet-exit Mach number listed in table 2 is $Ma_e = U_e/c_\infty$, where U_e is the jet-exit (inflow) bulk velocity and c_∞ denotes the ambient sound speed. The bulk velocity is formally defined in § 3.2.2. To simulate jets with identical inflow mean velocity for a perturbation type (laminar/turbulent), the same value of U_e is used in cases 1–5, 1T, 2T and 4T. Thus, the differences in Ma_e across those cases arise from the variation in c_∞ due to different ambient thermodynamic conditions. To examine the influence of p_∞ and Z at a fixed Ma_e, cases 2M and 4M are considered with same (laminar) inflow and ambient thermodynamic conditions as cases 2 and 4, respectively, but with U_e varied to obtain a Ma_e of 0.6, which is the value used in case 1.

Cases 1T, 2T and 4T examine the influence of inflow perturbations through comparisons against cases 1, 2 and 4, respectively. Numerical results from increasingly finer grid resolutions, denoted by $N_x \times N_y \times N_z$, are used to ensure grid convergence, as discussed in Appendix B. Results from the finest grid simulation of each case are discussed in § 4. The significance of factor $\mathcal{F}$ in table 2 is explained in § 2.3.

The governing equations are the set of conservation equations and the equation of state; this equation set is complemented by the transport properties.

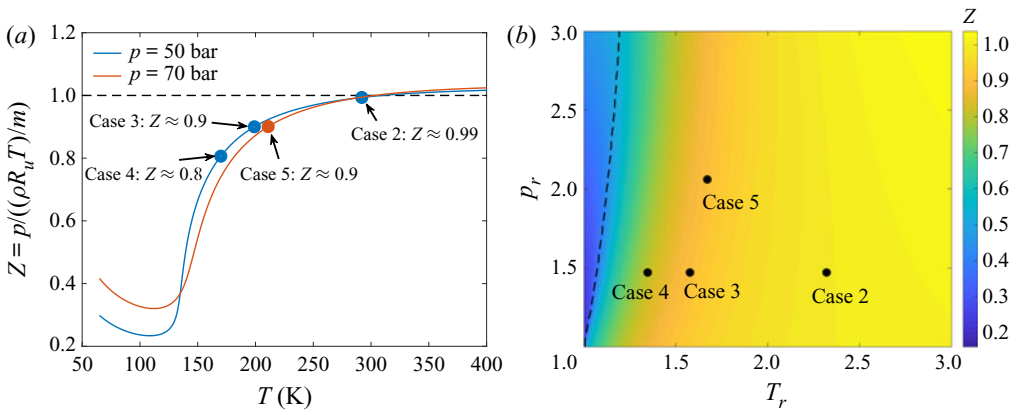

Figure 1. (*a*) Compressibility factor of N_2 at 50 and 70 bar pressure. Blue and red markers denote the ambient conditions for various high-p cases of table 2. (*b*) The p–T diagram of N_2 at supercritical conditions. The reduced temperature is $T_r = T/T_c$ and the reduced pressure is $p_r = p/p_c$, where the critical temperature $T_c = 126.2$ K and critical pressure $p_c = 33.98$ bar for N_2. The contour illustrates the distribution of Z and the black dashed line is the Widom line defined as the locus of the maximum isobaric heat capacity. Black markers denote the location of various high-p cases of table 2 on the thermodynamic state plane.

Case (description)	Z	$\beta_T \times 10^5$ (Pa^{-1})	$p_\infty\left(\beta_T - \frac{1}{p_\infty}\right)$	γ	$\beta_S \times 10^5$ (Pa^{-1})
1 (atm-p)	1	1.00000	0.000	1.4	0.71429
2 (high-p(50); $Z \approx 1$)	0.99	0.01995	−0.002	1.49	0.01339
3 (high-p(50); $Z \approx 0.9$)	0.9	0.02190	0.095	1.69	0.01296
4 (high-p(50); $Z \approx 0.8$)	0.8	0.02488	0.244	1.96	0.01269
5 (high-p(70); $Z \approx 0.9$)	0.9	0.01524	0.067	1.74	0.00876

Table 3. Values of various thermodynamic quantities for ambient conditions in cases 1 to 5. Cases 2M and 4M have same values as cases 2 and 4, respectively, and cases 1T, 2T and 4T have same values as cases 1, 2 and 4, respectively.

2.1. *Conservation equations*

The compressible flow equations for conservation of mass, momentum, energy and a passive scalar, solved in this study, are

$$\frac{\partial \rho}{\partial t} + \frac{\partial}{\partial x_j}[\rho u_j] = 0, \tag{2.3}$$

$$\frac{\partial}{\partial t}(\rho u_i) + \frac{\partial}{\partial x_j}[\rho u_i u_j + p\delta_{ij} - \sigma_{ij}] = 0, \tag{2.4}$$

$$\frac{\partial}{\partial t}(\rho e_t) + \frac{\partial}{\partial x_j}[(\rho e_t + p)u_j - u_i\sigma_{ij} + q_j] = 0, \tag{2.5}$$

$$\frac{\partial}{\partial t}(\rho \xi) + \frac{\partial}{\partial x_j}[\rho \xi\, u_j + J_j] = 0, \tag{2.6}$$

where t denotes the time, $(x_1, x_2, x_3) \equiv (x, y, z)$ are the Cartesian directions, subscripts i and j refer to the spatial coordinates, u_i is the velocity, p is the pressure, δ_{ij} is the Kronecker

delta, $e_t = e + u_i u_i/2$ is the total energy (i.e. internal energy, e, plus kinetic energy), $\xi \in [0, 1]$ is a passive scalar transported with the flow, σ_{ij} is the Newtonian viscous stress tensor components

$$\sigma_{ij} = \mu\left(2\mathcal{S}_{ij} - \frac{2}{3}\mathcal{S}_{kk}\delta_{ij}\right), \quad \mathcal{S}_{ij} = \frac{1}{2}\left(\frac{\partial u_i}{\partial x_j} + \frac{\partial u_j}{\partial x_i}\right), \tag{2.7a,b}$$

where μ is the viscosity, $\mathcal{S}_{ij}$ denotes the strain-rate tensor components and $q_j = -\lambda\,\partial T/\partial x_j$ and $J_j = -\mathscr{D}\,\partial\xi/\partial x_j$ are the heat flux and scalar diffusion flux in the j-direction, respectively. Here, λ is the thermal conductivity and $\mathscr{D} = \mu/Sc$ is the scalar diffusivity, where Sc denotes the Schmidt number. The injected fluid is assigned a scalar value, ξ, of 1, whereas the chamber fluid a value of 0. The passive scalar is not a physical species, and is only used as a surrogate quantity to track the injected fluid in this simple single-species flow.

2.2. *Equation of state*

For the near-atmospheric-p simulations (cases 1 and 1T), the perfect-gas equation of state (EOS) is applicable, given by

$$p = \frac{\rho R_u T}{m}. \tag{2.8}$$

For the high-p simulations (cases 2–5, 2M, 4M, 2T and 4T), the conservation equations are coupled with a Peng–Robinson (PR) EOS

$$p = \frac{R_u T}{(v_{PR} - b_{mix})} - \frac{a_{mix}}{\left(v_{PR}^2 + 2b_{mix}v_{PR} - b_{mix}^2\right)}. \tag{2.9}$$

The molar PR volume $v_{PR} = V - v_s$, where the molar volume $V = m/\rho$; v_s denotes the volume shift introduced to improve the accuracy of the PR EOS at high pressures (Harstad, Miller & Bellan 1997; Okong'o *et al.* 2002); a_{mix} and b_{mix} are functions of T and the molar fraction X_α (here $X_\alpha = 1$ because of single-species flows) and are obtained from expressions previously published (Sciacovelli & Bellan 2019, appendix B).

2.3. *Transport properties*

For the near-atmospheric-p simulations (cases 1 and 1T), the viscosity is modelled as a power law

$$\mu = \mu_R\left(\frac{T}{T_R}\right)^n, \tag{2.10}$$

with $n = 2/3$ and the reference viscosity being $\mu_R = \rho_e U_e D/Re_D$, where ρ_e and U_e are the jet-exit fluid density and jet-exit bulk velocity, respectively, and the reference temperature is $T_R = 293$ K. The thermal conductivity is $\lambda = \mu C_p/Pr$, where the Prandtl number $Pr = 0.7$ (as typical of 1 bar flows), the ratio of specific heats $\gamma = 1.4$ and the isobaric heat capacity $C_p = \gamma R_u/(\gamma - 1)$ is assumed.

For real gases in high-p simulations (cases 2–5, 2M, 4M, 2T and 4T), the physical viscosity, μ_{ph}, and thermal conductivity, λ_{ph}, are calculated using the Lucas method (Poling *et al.* 2001, chapter 9) and the Stiel–Thodos method (Poling *et al.* 2001, chapter 10), respectively, as a function of the local thermodynamic conditions. The computational viscosity, μ, and thermal conductivity, λ, are obtained by scaling μ_{ph} and λ_{ph} with a

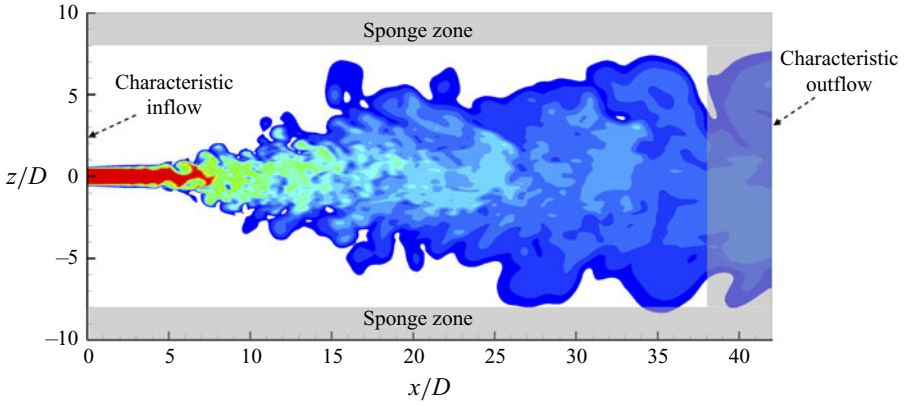

Figure 2. A two-dimensional schematic showing the extent of computational domain in axial and radial directions, and the boundary conditions applied at various boundaries.

factor $\mathcal{F} = \mu_R/\mu_{ph,\infty}$, i.e. $\mu = \mathcal{F}\mu_{ph}$ and $\lambda = \mathcal{F}\lambda_{ph}$, to allow simulations at the specified Re_D of 5000. The ambient physical viscosity ($\mu_{ph,\infty}$) is μ_{ph} at the pressure p_∞ and the temperature T_{ch} of respective cases. This procedure ensures that Pr, which is computed as a function of the local thermodynamic variables, has the physically correct value. The scalar diffusivity is obtained from $\mathscr{D} = \mu/Sc$, where unity Schmidt number is assumed in all cases. A validation of the transport and thermodynamic properties calculated from the above methods is presented in Appendix A.

The $\mathcal{F}$ values for all cases are listed in table 2. As an example, for case 1, $\mathcal{F} = \mu_R/\mu_{ph,\infty} \approx 6.5$ ($\mu_R = \rho_e U_e D/Re_D = 1.136 \times 10^{-4}$ Pa s and $\mu_{ph,\infty} = 1.757 \times 10^{-5}$ Pa s at $p_\infty = 1$ bar and $T_{ch} = 293$ K), and for case 2, $\mathcal{F} \approx 309.4$ ($\mu_R = 5.715 \times 10^{-3}$ Pa s and $\mu_{ph,\infty} = 1.847 \times 10^{-5}$ Pa s at $p_\infty = 50$ bar and $T_{ch} = 293$ K). The value of $\mathcal{F}$ is larger in case 2 compared with case 1 because of the larger density ρ_e at 50 bar that requires a larger μ_R for a fixed Re_D, while the physical viscosity $\mu_{ph,\infty}$ remains relatively unchanged with increase in p.

3. Numerical aspects

3.1. *Computational domain and numerical method*

For notation simplicity, $(x_1, x_2, x_3) \equiv (x, y, z)$ is adopted for axis labels; (u_1, u_2, u_3) denote the Cartesian velocity components, whereas (u, v, w) denote the axial, radial and azimuthal velocities. The computational domain extends to $42D$ in the axial (x-)direction and $20D$ in the y- and z-direction including the sponge zones, where D is the jet diameter, as shown schematically in an x–z plane of figure 2. The boundary conditions are discussed in § 3.2.1.

Spatial derivatives are approximated using the sixth-order compact finite-difference scheme and time integration uses the classical explicit fourth-order Runge–Kutta method. To avoid unphysical accumulation of energy at high wavenumbers, resulting from the use of non-dissipative spatial discretization, the conservative variables are filtered every five time steps using an explicit eighth-order filter (Kennedy & Carpenter 1994). The derivative approximations and filter operations over non-uniform stretched grids and polar grids (for post-processing and inflow generation) uses the generalized-coordinate formulation (e.g. Sharan 2016; Sharan, Pantano & Bodony 2018*b*).

To obtain the numerical solution, the conservation equations are first solved at each time step. With ρ and $e = e_t - u_i u_i/2$ obtained from the conservation equations and T computed iteratively from e, the EOS is used to calculate p (Okong'o *et al.* 2002).

3.2. *Boundary and inflow conditions*

3.2.1. *Boundary conditions*

The outflow boundary in the axial direction and all lateral boundaries have sponge zones (Bodony 2006) with non-reflecting outflow Navier–Stokes characteristic boundary conditions (NSCBC) (Poinsot & Lele 1992) at the boundary faces. Sponge zones at each outflow boundary have a width of 10 % of the domain length normal to the boundary face. The sponge strength at each boundary decreases quadratically with distance normal to the boundary. The performance of one-dimensional NSCBC (Poinsot & Lele 1992; Okong'o & Bellan 2002*a*) as well as its three-dimensional extension (Lodato, Domingo & Vervisch 2008) by inclusion of transverse terms were also evaluated without the sponge zones; they permit occasional spurious reflections into the domain and, therefore, the use of sponge zones was deemed necessary.

3.2.2. *Inflow conditions*

The role of initial/inflow conditions on free-shear flow development as well as the asymptotic (self-similar) state attained by the flow at atmospheric conditions is well recognized (Boersma *et al.* 1998; George & Davidson 2004; Sharan, Matheou & Dimotakis 2019). To examine the high-p jet-flow sensitivity to initial conditions, two types of inflows are considered, portraying either a jet exiting a smooth contracting nozzle or a jet exiting a long pipe. The former produces laminar inflow conditions with top-hat jet-exit mean velocity profile whereas the latter produces turbulent inflow conditions of fully developed pipe flow (Mi *et al.* 2001).

Cases 1–5, 2M and 4M employ laminar-inflow conditions with velocity profile at the inflow plane given by (e.g. Michalke 1984)

$$u(r) = \frac{U_e}{2}\left(1 - \tanh\left[\frac{r - r_0}{2\theta_0}\right]\right), \tag{3.1}$$

where $r = \sqrt{y^2 + z^2}$, the jet-exit radius is $r_0 = D/2$ and the momentum thickness is $\theta_0 = 0.04 r_0$. Small random perturbations with maximum amplitude of $0.004 U_e$, as listed in table 2, are superimposed on the inflow velocity profile to trigger jet-flow transition to turbulence. Perturbations are only added to the velocity field.

Cases 1T, 2T and 4T utilize turbulent-inflow conditions, typical of jets exiting a long pipe. The inflow is generated using the approach of Klein, Sadiki & Janicka (2003) modified to accommodate circular-pipe inflow geometry. This approach generates inflow statistics matching a prescribed mean velocity and Reynolds stress tensor, using the method of Lund, Wu & Squires (1998), with fine-scale perturbations possessing a prescribed spatial correlation length scale. The mean velocity and Reynolds stress profiles are here specified from the fully developed pipe flow DNS results of Eggels *et al.* (1994), where the Reynolds number, based on pipe diameter and bulk velocity, of 5300 is close to the jet Reynolds number of present study. The bulk velocity is defined as

$$U_b = \frac{1}{\pi\,(D/2)^2}\int_0^{D/2} 2\pi r u \,\mathrm{d}r. \tag{3.2}$$

For small values of θ_0 in (3.1), U_b for laminar-inflow cases is approximately equal to U_e; U_b in cases 1T, 2T and 4T is chosen to be equal to U_e of cases 1, 2 and 4, respectively, to allow fair one-to-one comparisons between them. Since U_e has the same value for cases 1–5, the bulk inflow velocity is approximately the same for cases 1–5, 1T, 2T and 4T. The choice of the correlation length scale determines the energy distribution among various spatial scales. Increasing the length scale leads to more dominant large-scale structures. Since the turbulent-inflow simulations are aimed at examining the influence of fully developed fine-scale inflow turbulence on jet statistics, a small isotropic value of $L/D = 0.1$ is assumed for the correlation length scale, this value being marginally larger than the finest scale in the velocity spectra of figure 7(*a–c*) in Eggels *et al.* (1994).

Figures 3 and 4 validate the turbulent-inflow implementation. In figure 3, the mean axial velocity from the present turbulent inflow is compared against the pipe flow DNS results (case DNS(E) of Eggels *et al.* 1994). Figure 4 illustrates a similar comparison of the root-mean-square (r.m.s.) axial-velocity fluctuation, u'_{rms}, and the Reynolds stress, $\overline{u'v'}$. The radial- and the azimuthal-velocity fluctuations, v'_{rms} and w'_{rms}, compare similarly well with the respective DNS profiles, and have been omitted for brevity. The overbar ($\bar{\bullet}$) denotes mean quantities, calculated by an average over time and azimuthal (θ) coordinate, given by a discrete approximation of

$$\bar{u}(x, r) = \frac{1}{2\pi} \int_0^{2\pi} \left(\frac{1}{(t_2 - t_1)} \int_{t_1}^{t_2} u(x, r, \theta, t)\, \mathrm{d}t \right) \mathrm{d}\theta. \tag{3.3}$$

For all results in this study, the time average is performed over time steps in the interval $t_1 = 1000 \leq tU_e/D \leq 4000 = t_2$. The r.m.s. fluctuations are calculated from

$$u'_{rms} = \sqrt{\left\langle \left\langle (u - \langle u \rangle_t)^2 \right\rangle_t \right\rangle_\theta} = \sqrt{\left\langle \left\langle u^2 \right\rangle_t - \langle u \rangle_t^2 \right\rangle_\theta}, \tag{3.4}$$

where $\langle \cdot \rangle_t$ and $\langle \cdot \rangle_\theta$ denote the time and azimuthal averages, respectively. Using the notation $\langle \cdot \rangle_t$ and $\langle \cdot \rangle_\theta$, (3.3) can be written as $\bar{u} = \langle \langle u \rangle_t \rangle_\theta$.

The method described in Klein *et al.* (2003) assumes a Cartesian grid with uniform spacing, where the periodic directions, along which averages are computed to determine mean quantities, are aligned with the Cartesian directions. The round-jet inflow considered here has circular orifice, where the azimuthal direction is periodic, which is not aligned with a Cartesian direction. Therefore, the fluctuations are computed on a polar grid and then interpolated to the Cartesian inflow grid.

4. Results

The influence of p_∞ and Z on the laminar-inflow jet behaviour is examined first in § 4.1. Then, the effects of p_∞ at a fixed Z of 0.9 are investigated in § 4.2. To differentiate between the effects of dynamic and thermodynamic compressibility, the influence of p_∞ and Z at a fixed Ma_e of 0.6 is studied in § 4.3. Finally, the effect of the inflow condition – laminar vs turbulent – is addressed in § 4.4, first as a baseline for the fully compressible atmospheric-p conditions in § 4.4.1 and then at high-p conditions in § 4.4.2.

To provide confidence in the numerical formulation and discretization, a validation of case 1, which obeys the perfect-gas EOS, against experimental results is presented in Appendix C; additionally, those results permit comparisons with high-p flow results where relevant.

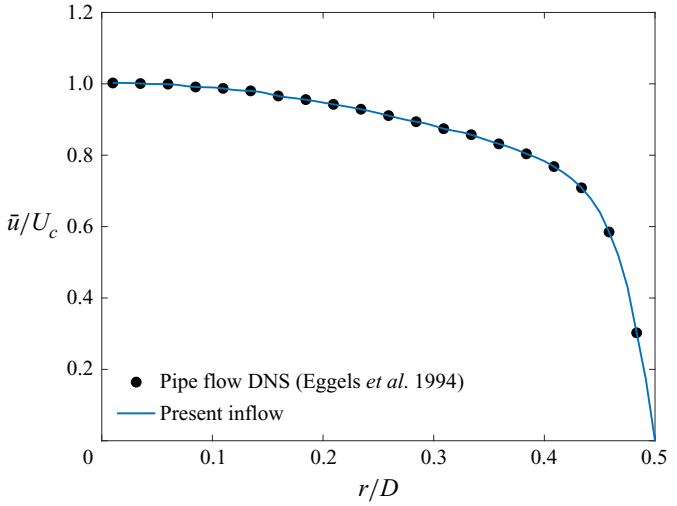

Figure 3. Inflow mean velocity normalized by the centreline velocity for the (pseudo-)turbulent inflow compared against the pipe flow DNS results of Eggels *et al.* (1994).

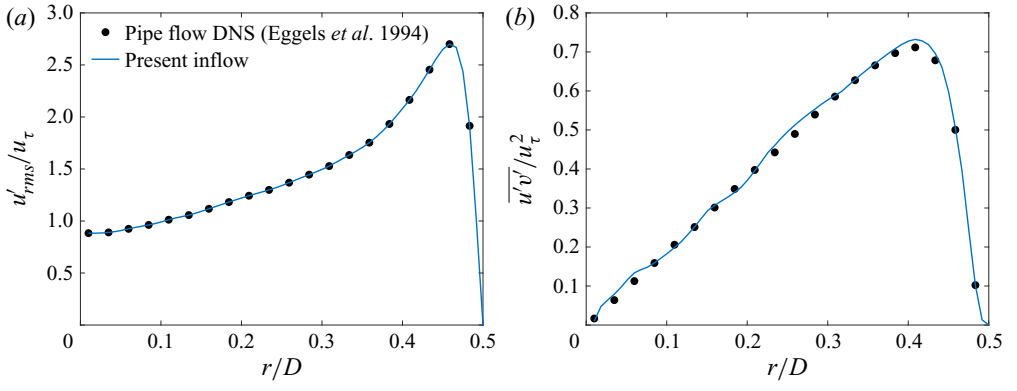

Figure 4. (*a*) The r.m.s. axial-velocity fluctuation, u'_{rms}, and (*b*) the Reynolds stress, $\overline{u'v'}$, normalized by the wall friction velocity, u_τ, from the (pseudo-)turbulent inflow compared against the pipe flow DNS results of Eggels *et al.* (1994).

4.1. *Effects of high pressure and compressibility factor*

The influence of p_∞ (from atmospheric to supercritical) on the jet-flow dynamics and mixing is here examined by comparing results from cases 1 and 2. Further, the effects of Z at supercritical p_∞ are examined by comparing results from cases 2 to 4. As indicated in table 2, in each case the fluid in the injected jet is as dense as the ambient (or chamber) fluid. The inflow bulk velocity, defined by (3.2), is the same for all cases. As a result, the inflow bulk momentum varies with change in inflow density.

4.1.1. *Mean axial velocity and spreading rate*

The inverse of the centreline mean axial velocity, $U_c(x)$ $(= \bar{u}(x, 0))$, normalized by the the jet-exit centreline velocity, U_0 $(= U_c(0))$, for cases 1 to 4 is presented in figure 5(*a*). For the laminar-inflow cases, which have a top-hat jet-exit mean velocity profile, $U_0 = U_e$, and

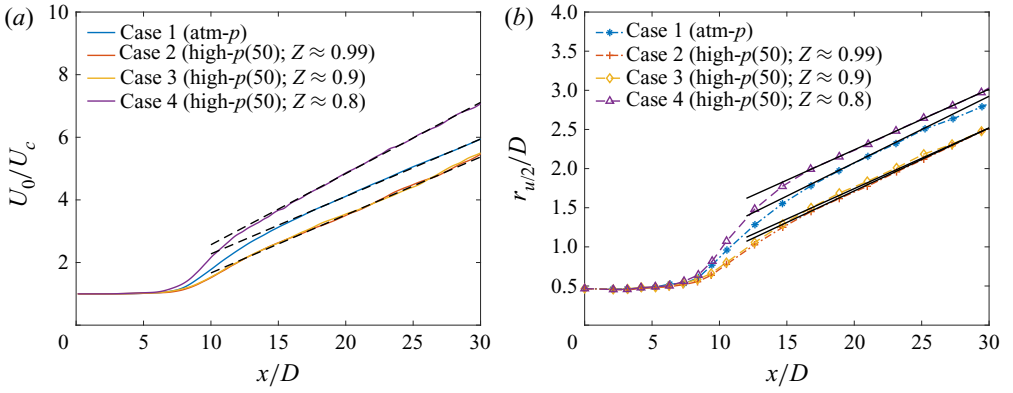

Figure 5. Case 1–4 comparisons: streamwise variation of the (*a*) inverse of centreline mean axial velocity (U_c) normalized by the jet-exit centreline velocity (U_0) and (*b*) velocity half-radius ($r_{u/2}$). The black dashed lines in (*a*) are given by (C1) using $B_u = 5.5$, $x_{0u} = -2.4D$ for case 1, $B_u = 5.4$, $x_{0u} = D$ for cases 2 and 3 and $B_u = 4.4$, $x_{0u} = -1.3D$ for case 4. The black solid lines in (b) are given by: $r_{u/2}/D = 0.085(x/D + 4.4)$ for case 1, $r_{u/2}/D = 0.0805(x/D + 1.3)$ for case 2, $r_{u/2}/D = 0.0775(x/D + 2.5)$ for case 3 and $r_{u/2}/D = 0.077(x/D + 8.9)$ for case 4.

since cases 1–5 use same U_e, U_0 is the same for all cases in figure 5(*a*). To our knowledge, figure 5(*a*) demonstrates for the first time that supercritical jets in the Mach-number range [0.58, 0.82], see table 2, attain self-similarity. This finding differs from the self-similarity observed in the low-Mach-number results of Ries *et al.* (2017), where the compressibility effects were ignored and the conservation equations did not use the pressure calculated from the EOS. In contrast, the fully compressible equations solved in the present study use the strongly nonlinear EOS which contributes to the thermodynamic-variable fluctuations, and self-similarity is not an obvious outcome.

In figure 5(*a*), the potential core length is approximately the same in all cases, but the velocity decay rates differ among cases in both the transition and the fully developed self-similar regions. In the transition region ($7 \lesssim x/D \lesssim 15$), the mean axial-velocity decay, assessed by the slope of the lines in figure 5(*a*), decreases with increasing p_∞ from 1 bar (case 1) to 50 bar (case 2), remains approximately the same with decrease in Z from 0.99 (case 2) to 0.9 (case 3), and increases significantly with further decrease in Z to 0.8 (case 4). In the self-similar region, the decay rates are quantified by the inverse of B_u, defined through (C1). The value of $1/B_u$ increases from 1/5.5 for case 1 to 1/5.4 for cases 2 and 3 and to 1/4.4 for case 4. Lines with slope $1/B_u$ are shown as black dashed lines in figure 5(*a*).

Figure 5(*b*) compares the velocity half-radius ($r_{u/2}$) among cases 1–4. In the transition region ($7 \lesssim x/D \lesssim 15$), the jet spread defined by the half-radius is larger for case 1 than case 2. The profiles are nearly identical for cases 2 and 3, and case 4 shows a significantly larger jet spread than the other cases. In the self-similar region, the linear spread can be described by the black solid lines of figure 5(*b*); the equations describing the solid lines are included in the figure caption. The self-similar spread rate decreases from case 1 to case 4. The decrease is relatively small from case 2 to case 3, and negligible from case 3 to case 4. Variation of ξ_c/ξ_0 and $r_{\xi/2}/D$ (not shown here for brevity) are similar to those of the velocity field in figure 5.

The decay of U_c, observed in figure 5(*a*), is a result of the concurrent processes of: (*a*) transfer of kinetic energy from the mean field to fluctuations, (*b*) transport of mean kinetic energy away from the centreline as more ambient fluid is entrained and

(c) mean viscous dissipation. These processes interact as follows. The entrainment of ambient fluid (initially at rest) into the jet enhances the momentum and kinetic energy of the ambient fluid. Transport of momentum/energy from the jet core facilitates the ambient-fluid entrainment and jet spread. As a result, a wider jet spread is associated with a larger decay in U_c. Therefore, the profiles for various cases look similar in figure 5(a,b). The production term of the t.k.e. equation quantifies the loss of mean kinetic energy to turbulent fluctuations and the mean strain rate magnitude is proportional to the mean viscous dissipation. The variation of U_c across various cases in figure 5(a) follows the variation of the t.k.e. production and the mean strain rate magnitude, as discussed in § 4.4.2.5.

The considerably larger decay of U_c in case 4 compared with other cases is at this point conjectured to be a coupled effect of its proximity to the Widom line, i.e. the thermodynamic state (see figure 1), and the mean strain rates generated in the flow, i.e. the dynamic state, that depends on the thermodynamic state, the inflow condition (laminar vs turbulent) and the jet-exit (inflow) Mach number. The proximity to the Widom line determines the departure from perfect-gas behaviour and the relative magnitude of pressure fluctuations across various cases, as further discussed in § 4.1.3. Prior to examining the role of pressure fluctuations in the unique behaviour of case 4, an evaluation of the consistency of U_c decay with the kinetic energy transfer from the mean field to fluctuations is performed by next examining the velocity fluctuations and their self-similarity.

4.1.2. *Velocity fluctuations and self-similarity*

The centreline r.m.s. axial-velocity fluctuation is depicted in figure 6 for cases 1–4 with two different normalizations. Since U_0 has the same value for cases 1–4, the normalization with U_0 compares the absolute fluctuation magnitude among various cases. On the other hand, the normalization with U_c shows the fluctuation magnitude with respect to the local mean value. Larger $u'_{c,rms}/U_c$ values are expected to indicate greater local transfer of mean kinetic energy to fluctuations. Accordingly, larger $u'_{c,rms}/U_c$ in figure 6 should imply a higher slope (U_c decay rate) in the corresponding region in figure 5(a). Case 4, which has the largest $u'_{c,rms}/U_c$ among all cases in both the transition and the self-similar region, also exhibits largest slopes (decay rates) in figure 5(a). Case 1 has larger $u'_{c,rms}/U_c$ than cases 2 and 3 in the transition region and, accordingly, higher decay rates in that region in figure 5(a). In the self-similar region, $u'_{c,rms}/U_c$ in cases 2 and 3 are marginally larger than in case 1, and, accordingly, the self-similar U_c decay rates of cases 2 and 3 are marginally higher. This confirms that the decay in U_c is consistently reflected in the magnitude of $u'_{c,rms}/U_c$.

The linear mean axial-velocity decay and the linear jet-spread rate, downstream of the transition region, in figure 5 indicate the self-similarity of the mean axial velocity. The self-similarity of mean axial velocity and Reynolds stresses is further examined from their radial variation in figure 7. Figure 7(a) shows the radial profiles of $\bar{u}/U_c$ from cases 1–4 at $x/D \approx 25$ (solid lines) and 30 (dashed lines). In all cases, profiles at the two axial locations show minimal differences, suggesting that $\bar{u}/U_c$ has attained self-similarity. The self-similar mean velocity/scalar profile is commonly expressed as (e.g. Mi *et al.* 2001; Xu & Antonia 2002)

$$\bar{u}(x, r) = U_c\,(x) f\,(\eta)\,, \quad \bar{\xi}(x, r) = \xi_c\,(x)\, g\,(\eta)\,, \tag{4.1a,b}$$

where $f(\eta)$ and $g(\eta)$ are similarity functions, often described by Gaussian distributions,

$$f\,(\eta) = \exp(-A_u \eta^2), \quad g\,(\eta) = \exp(-A_\xi \eta^2), \tag{4.2a,b}$$

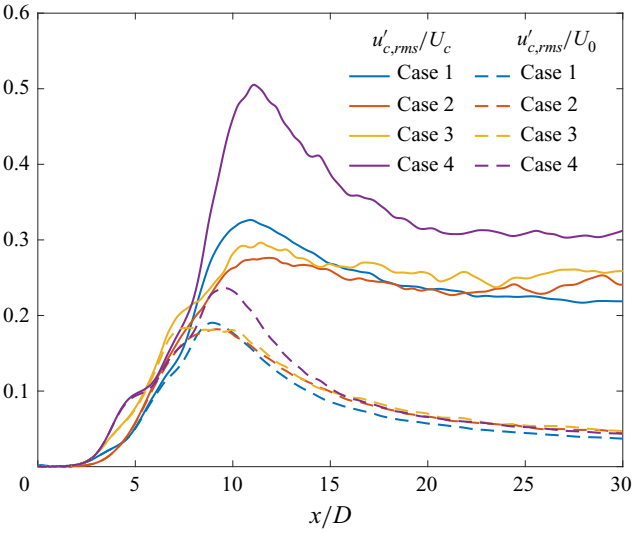

Figure 6. Case 1–4 comparisons: streamwise variation of the centreline r.m.s. axial-velocity fluctuation ($u'_{c,rms}$) normalized by the centreline mean value, U_c, and jet-exit mean value, U_0.

where A_u and A_ξ are constants, here determined from a least-squares fit of the simulation data. The least-squares procedure applied to $x/D \approx 30$ profiles of figure 7(*a*) yields $A_u = 79.5$ for cases 1 and 2, $A_u = 77.2$ for case 3 and $A_u = 64.4$ for case 4. Thus, increasing p from 1 bar (case 1) to 50 bar (case 2) has minimal influence on the radial variation of the self-similar axial-velocity profile. A decrease in Z from 0.99 (case 2) to 0.9 (case 3) and then to 0.8 (case 4) at $p_\infty = 50$ bar increases $\bar{u}/U_c$ at a fixed η.

The radial variation of normalized r.m.s. velocity fluctuations at $x/D \approx 25$ and 30 are compared for cases 1–4 in figure 7(*b–e*). In all panels, the profiles at $x/D \approx 25$ (solid lines) and 30 (dashed lines) show minimal difference, and hence the r.m.s. velocity fluctuations can be considered self-similar around $x/D \approx 25$. The value of u'_{rms}/U_c, shown in figure 7(*b*), increases in the vicinity of the centreline with an increase in p_∞ from 1 bar (case 1) to 50 bar (case 2), but the differences diminish with increase in η. A decrease in Z from 0.99 (case 2) to 0.9 (case 3) marginally increases u'_{rms}/U_c at both small and large η. Further decrease in Z from 0.9 (case 3) to 0.8 (case 4) shows significant increase in u'_{rms}/U_c at all η-locations. The value of $u'_{rms}/u'_{c,rms}$, plotted in figure 7(*c*) shows that the fluctuations increase with radial distance near the centreline in case 1, with maximum at $\eta \approx 0.07$. The location of the maximum (in terms of η) recedes towards the centreline progressively in cases 2 and 3. Case 4 does not exhibit an off-axis maximum and $u'_{rms}/u'_{c,rms}$ decreases monotonically with η, highlighting the peculiarity with respect to cases 2 and 3.

Additionally, v'_{rms}/U_c and w'_{rms}/U_c, shown in figures 7(*d*) and 7(*e*), respectively, increase from case 1 to 4. The increase is marginal from case 1 to 3, but significant in case 4. Axisymmetry of a round-jet flow requires that v'_{rms} and w'_{rms} be equal at the centreline, which is nearly true for all cases in figures 7(*d*) and 7(*e*). Comparable profiles of $\overline{u'v'}/U_c^2$ in figure 7(*f*) at $x/D \approx 25$ and 30 suggest that $\overline{u'v'}/U_c^2$ attains self-similarity around $x/D \approx 25$ in cases 1–4. The value of $\overline{u'v'}/U_c^2$ is similar for cases 1–4 in the vicinity of the centreline but the profiles differ at larger η, where case 4 values are considerably larger than the other cases.

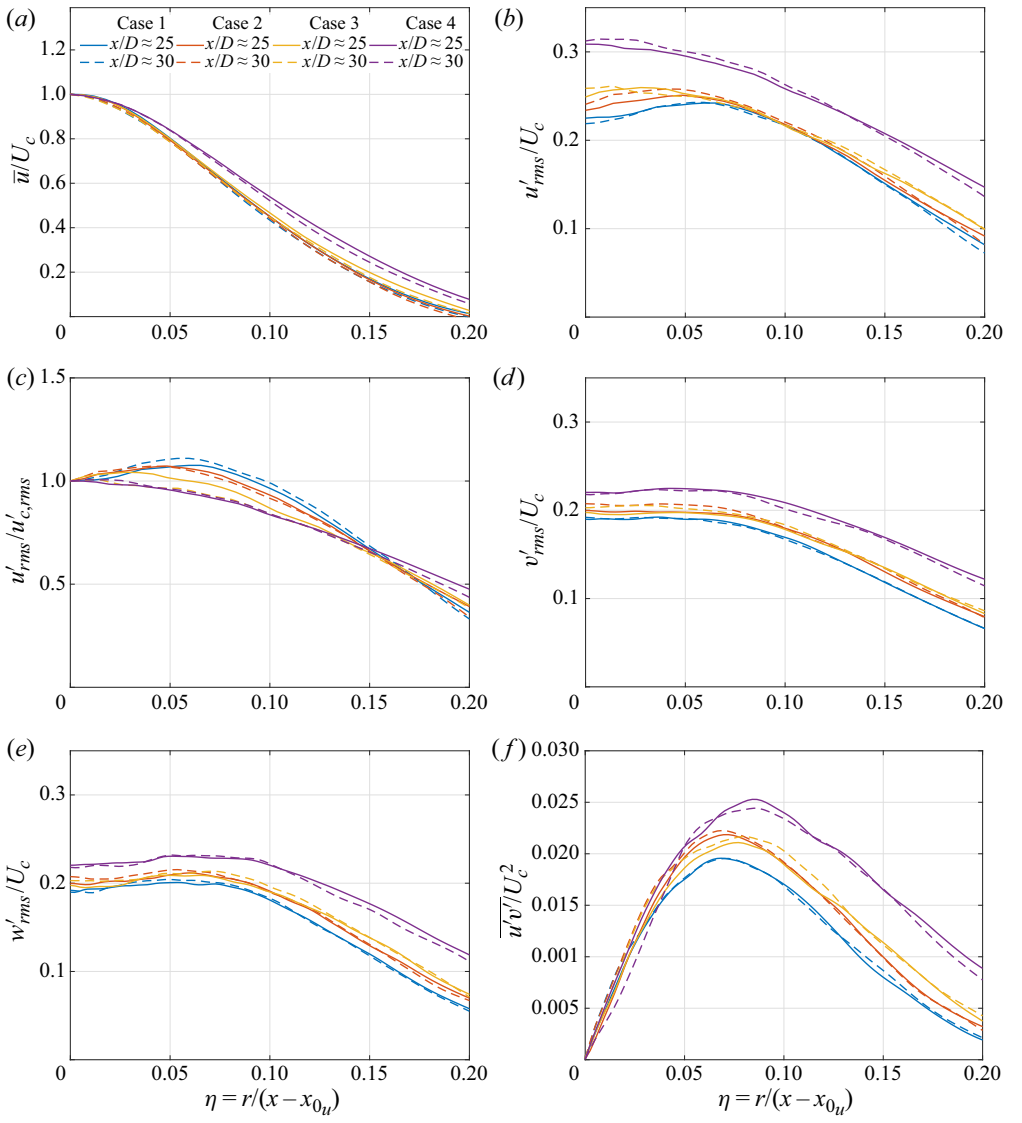

Figure 7. Case 1–4 comparisons: radial profiles of (*a*) mean axial velocity ($\tilde{u}$) normalized by the centreline mean axial velocity (U_c), (*b*) r.m.s. axial velocity fluctuations (u'_{rms}) normalized by the centreline mean axial velocity, (*c*) r.m.s. axial-velocity fluctuations (u'_{rms}) normalized by the centreline r.m.s. axial velocity fluctuations ($u'_{c,rms}$), (*d*) normalized r.m.s. radial velocity fluctuations (v'_{rms}), (*e*) normalized r.m.s. azimuthal-velocity fluctuations (w'_{rms}) and (*f*) normalized Reynolds stress ($\overline{u'v'}$) at various axial locations. The legend is the same for all plots.

4.1.3. *Pressure and density fluctuations, pressure–velocity correlation and third-order velocity moments*

The differences in mean axial velocity for various cases, observed in figure 5, are consistent with the differences in velocity fluctuations, examined in the previous section. Larger velocity fluctuations imply greater transfer of energy from the mean field to fluctuations, resulting in greater decay of mean velocity. The differences in velocity

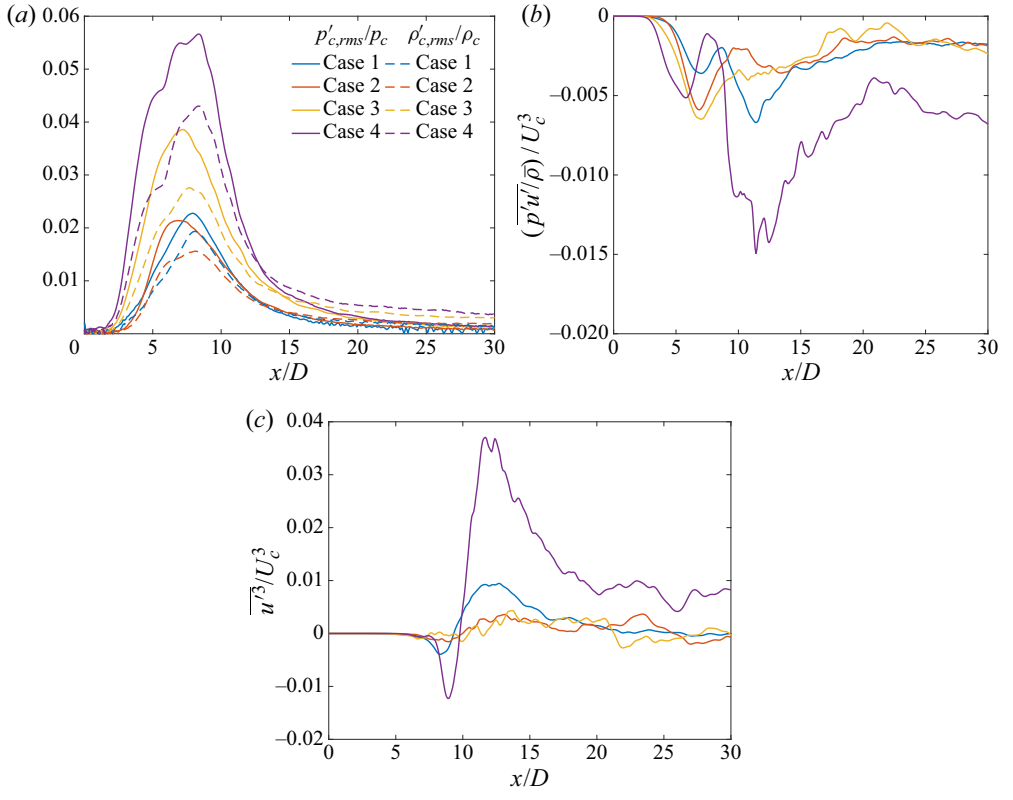

Figure 8. Case 1–4 comparisons: streamwise variation of the (*a*) centreline r.m.s. pressure and density fluctuations, denoted by $p'_{c,rms}$ and $\rho'_{c,rms}$, respectively, normalized by the centreline mean pressure (p_c) and density (ρ_c), respectively; (*b*) normalized fluctuating pressure–axial-velocity correlation ($\overline{p'u'}/\bar{\rho}U_c^3$), and (*c*) normalized third-order velocity moment ($\overline{u'^3}/U_c^3$).

fluctuations with p_∞ and Z, however, remain to be explained, and this topic is addressed next.

Gradients of the pressure/density fluctuations, pressure–velocity correlations and third-order velocity moments determine the transport terms in the Reynolds stress and t.k.e. equations (e.g. Panchapakesan & Lumley 1993; Hussein *et al.* 1994), and hence their role in causing the differences observed in velocity fluctuations of cases 1–4 (figures 6 and 7) is examined in figures 8–10.

The axial variation of the centreline r.m.s. pressure and density fluctuations normalized using centreline mean values, p_c and ρ_c, respectively, are compared in figure 8(*a*) for cases 1–4. The normalization provides information on the fluctuation magnitude with respect to local pressure and density (thermodynamic state). In all cases, $p'_{c,rms}/p_c$ and $\rho'_{c,rms}/\rho_c$ have a maximum in the transition region and asymptote to a constant value in the self-similar region. The value of $p'_{c,rms}/p_c$ exceeds $\rho'_{c,rms}/\rho_c$ in the transition region and *vice versa* in the self-similar region. Increasing p_∞ from 1 bar (case 1) to 50 bar (case 2) slightly reduces $p'_{c,rms}/p_c$ (shown as solid lines) and $\rho'_{c,rms}/\rho_c$ (shown as dashed lines) at all centreline locations, whereas decreasing Z from 0.99 (case 2) to 0.9 (case 3) and then to 0.8 (case 4) increases $p'_{c,rms}/p_c$ and $\rho'_{c,rms}/\rho_c$ significantly. The variation of $p'_{c,rms}/p_c$ and $\rho'_{c,rms}/\rho_c$ follows the variation of $p_\infty(\beta_T - 1/p_\infty)$, listed in table 3, that measures the

real-gas effects at ambient thermodynamic condition. The large value of $p_\infty(\beta_T - 1/p_\infty)$ for case 4 concurs with the large $p'_{c,rms}/p_c$ and $u'_{c,rms}/U_c$ observed in case 4, a fact which indicates that the large U_c decay and jet spread in case 4 are a result of the real-gas effects due to its proximity to the Widom line.

While $p_\infty(\beta_T - 1/p_\infty)$ explains the behaviour of case 4 with respect to other cases, it does not explain the behaviour of case 3 with respect to case 1 in the transition region of the flow. Larger $p_\infty(\beta_T - 1/p_\infty)$ in case 3 may suggest larger $p'_{c,rms}/p_c$ and $u'_{c,rms}/U_c$ in case 3 compared with case 1. But, while $p'_{c,rms}/p_c$ is larger in case 3 than in case 1 at all axial locations, $u'_{c,rms}/U_c$ in case 1 exceeds case 3 in the transition region, resulting in larger U_c decay and jet spread in case 1 than in case 3. To understand this discrepancy, the centreline variation of fluctuating pressure–axial-velocity correlation, $\overline{p'u'}$, whose axial gradient determines t.k.e. diffusion due to pressure fluctuation transport in the t.k.e. equation, is illustrated in figure 8(*b*). Large local changes in $\overline{p'u'}$ increase the turbulent transport term magnitude in the t.k.e. equation. The $\overline{p'u'}$ values are non-positive at all centreline locations for all cases, implying that a positive pressure fluctuation (higher than the mean) is correlated with negative velocity fluctuation (lower than the mean) and *vice versa*. The $(\overline{p'u'}/\bar{\rho})/U_c^3$ profiles in figure 8(*b*) for all cases have a local minimum in the near field $5 \lesssim x/D \lesssim 9$ and downstream of that minimum, the variations in $(\overline{p'u'}/\bar{\rho})/U_c^3$ are much larger in case 4 compared with case 1, which itself exhibits larger variations than in cases 2 and 3. In the region $9 \lesssim x/D \lesssim 15$, $(\overline{p'u'}/\bar{\rho})/U_c^3$ profiles exhibit distinct minima (with large negative values) in cases 1 and 4, whereas the profiles of cases 2 and 3 smoothly approach a near-constant value. The larger variation of $(\overline{p'u'}/\bar{\rho})/U_c^3$ in this region in cases 1 and 4 coincides with the larger U_c decay and jet spread in figure 5 and larger $u'_{c,rms}/U_c$ in figure 6 for those cases. This indicates that higher $p'_{c,rms}/p_c$ does not guarantee higher $u'_{c,rms}/U_c$, instead $u'_{c,rms}/U_c$ follows the behaviour of $(\overline{p'u'}/\bar{\rho})/U_c^3$, whose axial gradient determines the turbulent transport term in the Reynolds stress equation governing $u'_{c,rms}$ and the t.k.e. equation. In § 4.4.2.5, it is further observed that the variations in t.k.e. turbulent transport agrees with the variations in the t.k.e. production resulting from the structural change in turbulence due to thermodynamic conditions. The differences in $u'_{c,rms}/U_c$ behaviour of cases 3 and 4 with respect to case 1 suggests that a relatively large change in thermodynamic condition from a perfect gas, as in case 4, is required to effect a large change in $u'_{c,rms}/U_c$. On the centreline, the fluctuating pressure–radial-velocity correlation, $\overline{p'v'}$, is null.

The centreline variation of $\overline{u'^3}/U_c^3$ is examined in figure 8(*c*) for cases 1–4. The increase in p_∞ from 1 bar (case 1) to 50 bar (case 2) reduces the overall axial variations of $\overline{u'^3}/U_c^3$, whereas the decrease in Z from 0.99 (case 2) to 0.9 (case 3) at 50 bar pressure has minimal influence on $\overline{u'^3}/U_c^3$ behaviour. Further decrease of Z to 0.8 (case 4) significantly enhances variations in $\overline{u'^3}/U_c^3$, indicating the significance of its gradient in the t.k.e. equation with proximity to the Widom line. Similar to figure 8(*b*), regions of large variations in $\overline{u'^3}/U_c^3$ concur with the regions of large changes in mean axial velocity and large velocity fluctuations seen in figures 5 and 6, respectively.

To complete the physical picture, the radial variation of fluctuating pressure–velocity correlations and third-order velocity moments at $x/D \approx 25$ and 30 from cases 1–4 are compared in figures 9 and 10, respectively. Both $\overline{p'u'}/\bar{\rho}/U_c^3$ and $(\overline{p'v'}/\bar{\rho})/U_c^3$ exhibit negative values at all radial locations. $(\overline{p'u'}/\bar{\rho})/U_c^3$ peaks in absolute magnitude at

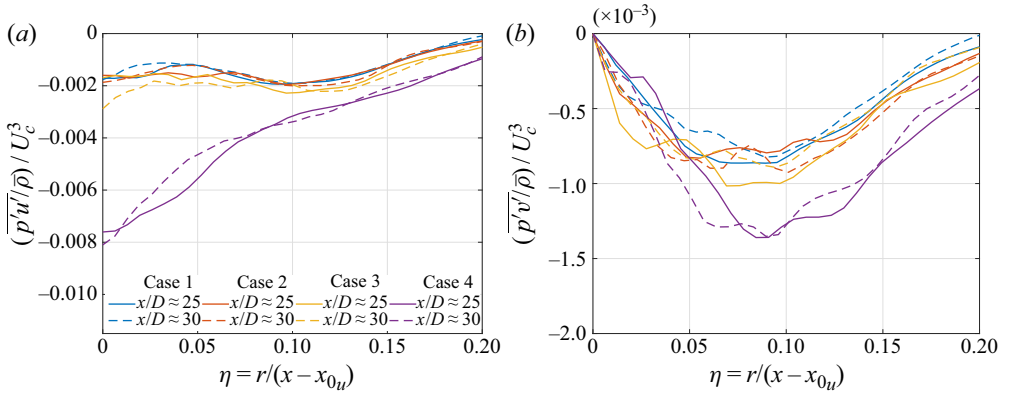

Figure 9. Case 1–4 comparisons: radial profiles of the (*a*) normalized pressure–axial-velocity correlation and (*b*) normalized pressure–radial-velocity correlation at $x/D \approx 25$ and 30.

the centreline, whereas the peak of $(\overline{p'v'}/\bar{\rho})/U_c^3$ lies off axis. The radial variation of $(\overline{p'u'}/\bar{\rho})/U_c^3$ in case 4 is significantly larger than in other cases at all radial locations, implying greater normalized t.k.e. diffusion flux due to pressure fluctuation transport by axial-velocity fluctuations. The normalized radial t.k.e. diffusion flux from pressure fluctuation transport, $(\overline{p'v'}/\bar{\rho})/U_c^3$, is similar near the centreline for all cases but larger in magnitude in case 4 for $\eta \gtrsim 0.075$, indicating greater radial t.k.e. transport in case 4 that enhances entrainment and mixing at the edges of the jet shear layer. Similarly, the third-order velocity moments, representing the t.k.e. diffusion fluxes due to the transport of Reynolds stresses by the fluctuating velocity field, depicted in figure 10, highlight the difference in behaviour in case 4 compared with other cases. All non-zero third-order moments from cases 1–4 together with the experimental profiles from Panchapakesan & Lumley (1993) are shown in the figure; the Panchapakesan & Lumley (1993) experiments measured all third-order moments except $\overline{v'w'^2}$. Aside from the large flux values in case 4, a noticeable feature in correlations $\overline{u'^2v'}$, $\overline{u'v'^2}$ and $\overline{u'w'^2}$ is their negative values near the centreline. The negative $\overline{u'^2v'}$ indicates a radial flux of the axial component of t.k.e., $\overline{u'^2}$, towards the centreline. The smaller region of negative values with decrease in Z from case 2 to case 4 indicates a smaller radial flux towards the centreline and a dominant radially outward transport of $\overline{u'^2}$.

4.1.4. *Passive scalar mixing*

To assess whether there are mixing differences among cases 1–4 emulating those of the velocity field, the one-point scalar probability density function (p.d.f.) is examined in figure 11 at various centreline locations. The p.d.f., $\mathcal{P}(\xi)$, is defined such that

$$\int_0^1 \mathcal{P}(\tilde{\xi})\,\mathrm{d}\tilde{\xi} = 1 \quad \text{and} \quad \bar{\xi} = \int_0^1 \tilde{\xi}\mathcal{P}(\tilde{\xi})\,\mathrm{d}\tilde{\xi}. \tag{4.3a,b}$$

Comparisons between cases 1 and 2, shown in figure 11(*a*), evaluate the effect of a p_∞ increase at approximately same Z value. At $x/D \approx 5$, the centreline contains pure jet fluid ($\xi = 1$) in both cases. The potential core closes downstream of $x/D \approx 5$, and the

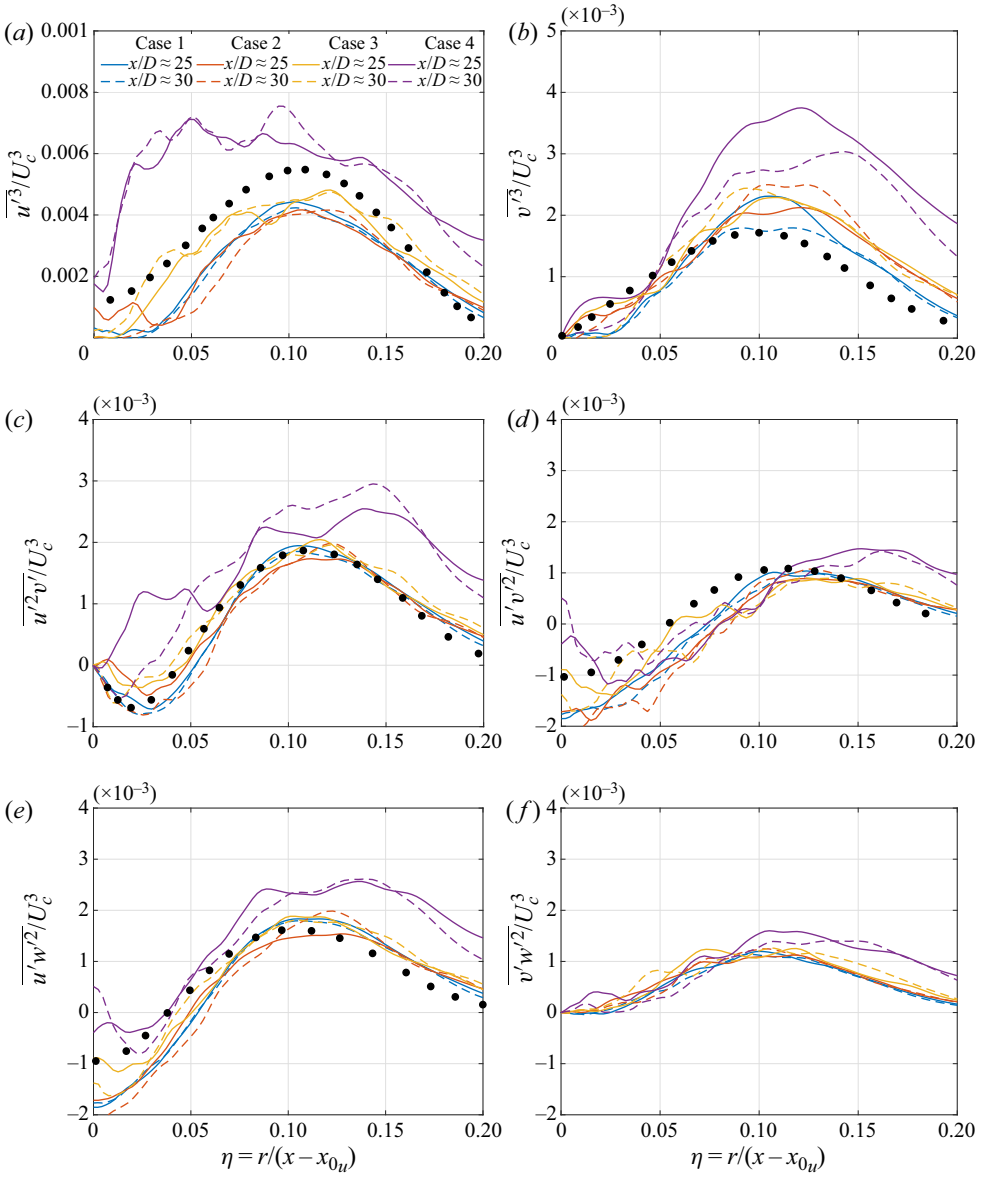

Figure 10. Case 1–4 comparisons: radial profiles of the normalized third-order velocity moments; (*a*) $\overline{u'^3}/U_c^3$, (*b*) $\overline{v'^3}/U_c^3$, (*c*) $\overline{u'^2v'}/U_c^3$, (*d*) $\overline{u'v'^2}/U_c^3$, (*e*) $\overline{u'w'^2}/U_c^3$ and (*f*) $\overline{v'w'^2}/U_c^3$. The black markers • show profiles from the experiments of Panchapakesan & Lumley (1993).

p.d.f. at $x/D \approx 8$ in both cases shows a wide spread with mixed-fluid concentration in the range $0.3 \lesssim \xi \lesssim 1$. Velocity/pressure statistics in the transition region of cases 1 and 2 differ significantly, as observed in figures 5, 6 and 8(*a*). Similarly, $\bar{\xi}$ and ξ'_{rms} vary in the transition region, yielding differences in mixed-fluid composition and $\mathcal{P}(\xi)$. In the transition region, the mean scalar concentration decays at a faster rate in case 1 than in case 2, as shown in figure 12(*a*). As a result, downstream of $x/D \approx 10$, the p.d.f. peaks are closer to the jet pure fluid concentration ($\xi = 1$) in case 2 than in case 1, indicating lesser

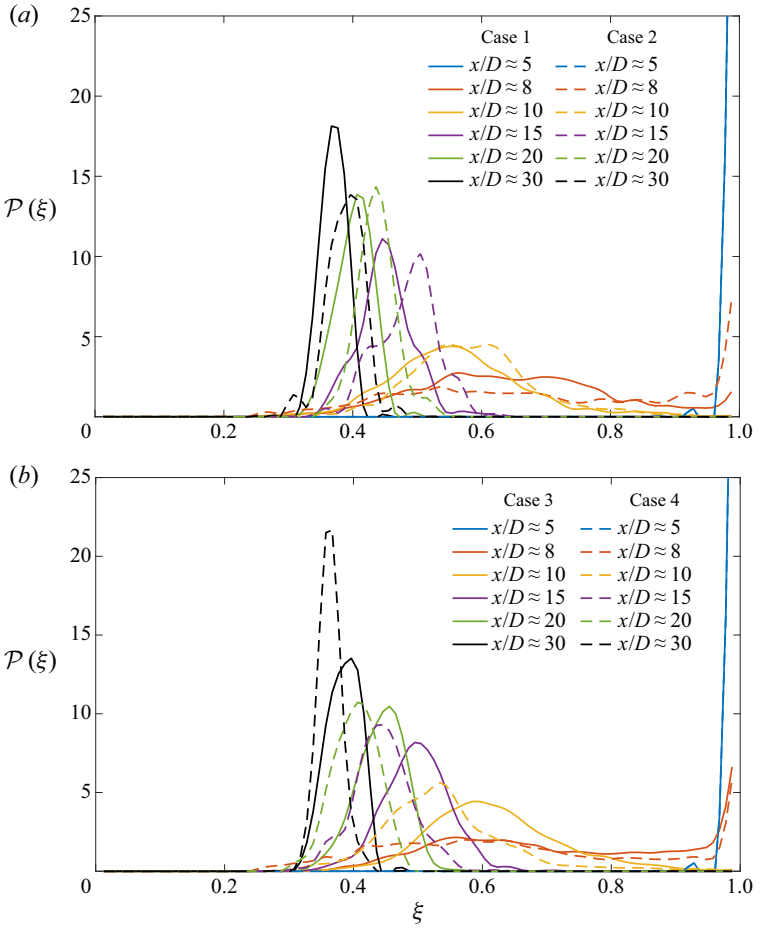

Figure 11. Scalar p.d.f., $\mathcal{P}(\xi)$, at various centreline axial locations for (*a*) cases 1 and 2, and (*b*) cases 3 and 4.

mixing in case 2 compared with case 1. For $x/D \geq 10$, the absolute scalar fluctuations $\xi'_{c,rms}/\xi_0$ are slightly larger in case 2 than in case 1, despite smaller normalized local fluctuation $\xi'_{c,rms}/\xi_c$ in case 2 between $10 \geq x/D \geq 20$, as shown in figure 12(*b*). Larger $\xi'_{c,rms}/\xi_0$ implies wider p.d.f. profiles with smaller peaks, indicating larger fluctuations in the mixed-fluid composition and, hence, greater mixing in case 2 compared with case 1. However, due to the large jet width downstream of $x/D \approx 15$, the scalar fluctuations at the centreline mix the already (partially) mixed fluid in the vicinity of the centreline and not the pure ambient fluid with the jet fluid. As a result, the p.d.f. peaks showing the mean mixed-fluid concentration continue to be closer to the jet pure fluid concentration ($\xi = 1$) in case 2 than in case 1.

Figure 11(*b*) compares the scalar p.d.f. from cases 3 and 4 to examine the effect of Z on mixing behaviour at supercritical pressure. Analogous to figure 11(*a*), the p.d.f. profiles at $x/D \approx 5$ and 8 are largely similar between the two cases. Differences in peak scalar value, representing the mean concentration, arise in the transition region, consistent with the observations in figure 12. Large scalar fluctuations around $x/D \approx 10$ in case 4 compared with case 3 lead to greater mixing in case 4 in the transition region, resulting in the p.d.f. peaks that are closer to the jet pure fluid concentration ($\xi = 1$) in case 3 than in case 4.

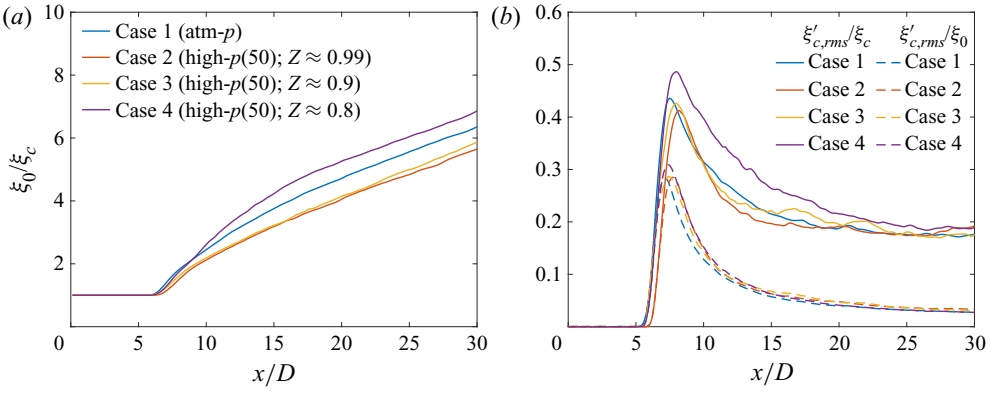

Figure 12. Case 1–4 comparisons: streamwise variation of the (*a*) inverse of centreline scalar concentration (ξ_c) normalized by the jet-exit centreline value (ξ_0) and (*b*) centreline r.m.s. scalar fluctuation ($\xi'_{c,rms}$) normalized by the centreline mean value, ξ_c, and jet-exit mean value, ξ_0.

At locations downstream of $x/D \approx 15$, the slightly larger $\xi'_{c,rms}/\xi_0$ in case 3 compared with case 4 leads to wider p.d.f. profiles with smaller peaks in case 3. However, the large jet width downstream of $x/D \approx 15$ causes mixing of the already (partially) mixed fluid in the vicinity of the centreline and, hence, the p.d.f. peaks continue to be closer to the jet pure fluid concentration in case 3 than in case 4.

4.1.5. *Summary*

The examination of the influence of p_∞ and Z on flow statistics in laminar-inflow jets at fixed Re_D yields several conclusions. The velocity statistics (mean and fluctuations) attain self-similarity in high-p compressible jets. The flow exhibits sensitivity to p_∞ and Z in the transition as well as the self-similar region, with larger differences observed in the transition region. The normalized pressure and density fluctuations in the flow follow the behaviour of the non-dimensional quantity $p_\infty(\beta_T - 1/p_\infty)$, listed in table 3, that provides a measure other than Z to estimate departure from perfect gas. Proximity of the ambient flow conditions to the Widom line increases $p_\infty(\beta_T - 1/p_\infty)$ and enhances the normalized pressure and density fluctuations in the flow, especially in the transition region. The velocity behaviour (mean and fluctuations) can be explained in terms of the spatial variation of the normalized pressure–velocity correlations and third-order velocity moments that determine the transport terms in the t.k.e. equation. An increase in velocity fluctuations also enhances the scalar fluctuations, leading to greater centreline mixing in case 4 compared with the other cases.

4.2. *Effects of supercritical pressure at a fixed compressibility factor*

The above analysis examined the effects of Z at a fixed supercritical p_∞. To examine its counterpart, the influence of p_∞ at a fixed Z of 0.9 is studied here by comparing results between cases 3 and 5 (see table 2). The value of $p_\infty(\beta_T - 1/p_\infty)$ is slightly larger in case 3 compared with case 5, a fact which according to the results of § 4.1 should lead to larger local pressure/density fluctuations in case 3.

The differences in the centreline profiles of the mean axial velocity and mean scalar concentration between cases 3 and 5, presented in figure 13(*a*), are minimal in the transition region and they diminish in the self-similar region. Similar to figure 13(*a*),

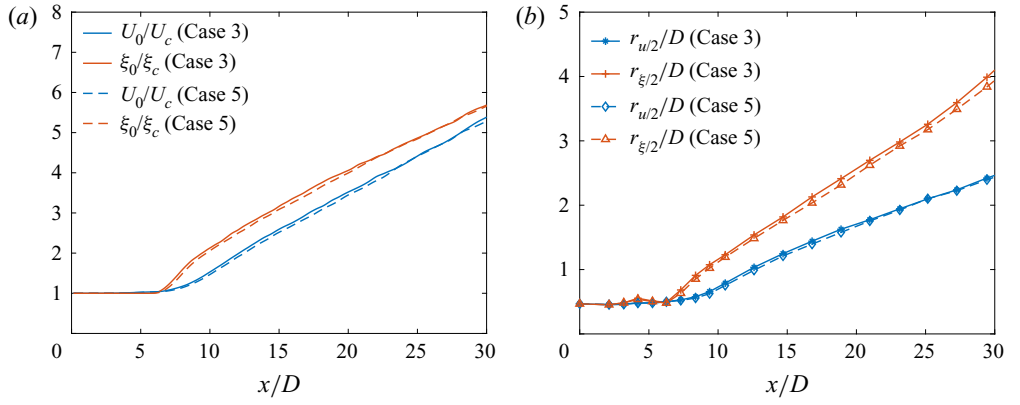

Figure 13. Case 3 and 5 comparisons: streamwise variation of the (*a*) inverse of centreline mean axial velocity (U_c) and scalar (ξ_c) normalized by the jet-exit centreline values U_0 and ξ_0, respectively, and (*b*) velocity and scalar half-radius ($r_{u/2}$ and $r_{\xi/2}$).

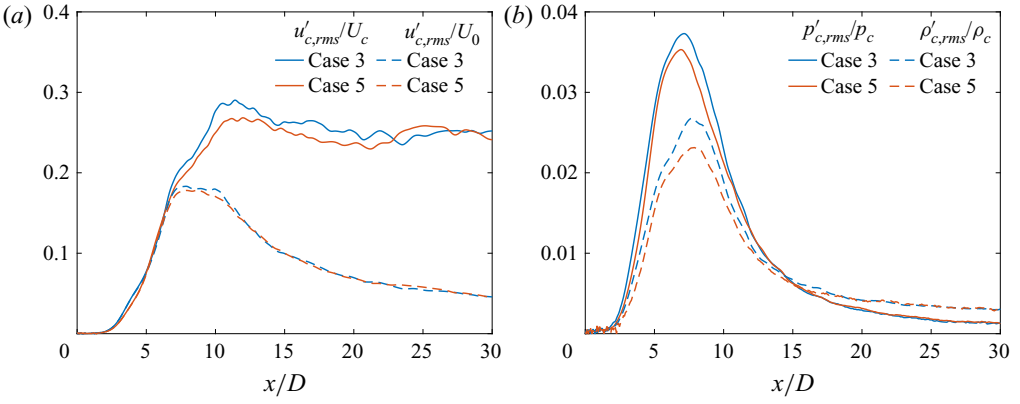

Figure 14. Case 3 and 5 comparisons: streamwise variation of (*a*) the centreline r.m.s. axial-velocity fluctuations ($u'_{c,rms}$) normalized by the centreline mean axial velocity (U_c) and centreline jet-exit axial velocity (U_0), and (*b*) the centreline r.m.s. pressure and density fluctuations, denoted by $p'_{c,rms}$ and $\rho'_{c,rms}$, respectively, normalized by the centreline mean pressure (p_c) and density (ρ_c), respectively.

minor differences are observed in the velocity half-radius ($r_{u/2}$), shown in figure 13(*b*), between cases 3 and 5. In comparison, small but noticeable differences are observed in scalar half-radius ($r_{\xi/2}$), where the jet spread in case 3 is slightly larger than that in case 5.

To further examine the differences between case 3 and case 5, a comparison of the normalized centreline velocity, pressure and density fluctuations is shown in figure 14. Centreline r.m.s. axial-velocity fluctuations with two different normalizations are compared in figure 14(*a*); U_0 has the same value for cases 3 and 5, therefore, $u'_{c,rms}/U_0$ compares the absolute fluctuation magnitude. In contrast, $u'_{c,rms}/U_c$ depicts the fluctuation magnitude with respect to local mean value. Case 3 exhibits slightly larger $u'_{c,rms}/U_c$ and $u'_{c,rms}/U_0$ in the transition region than case 5, as expected from the slightly greater U_c decay in case 3 than case 5 in figure 13. The normalized pressure and density fluctuations, illustrated in figure 14(*b*), show similarly that $p'_{c,rms}/p_c$ and $\rho'_{c,rms}/\rho_c$ are larger in case 3 than case 5 in the transition region of the flow.

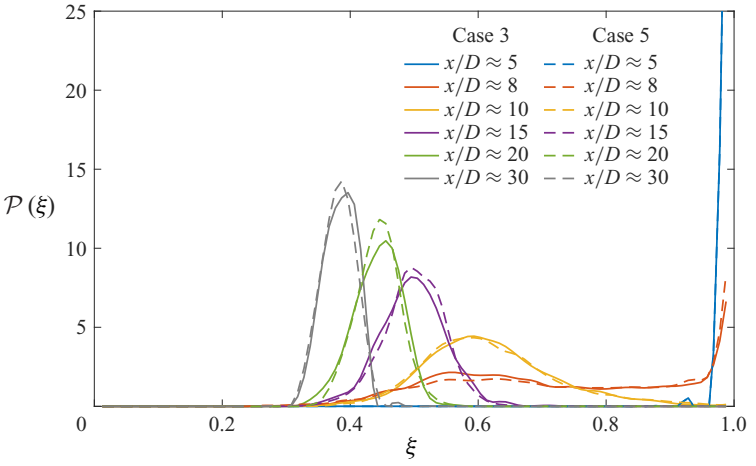

Figure 15. Case 3 and 5 comparisons: scalar p.d.f., $\mathcal{P}(\xi)$, at various centreline axial locations.

Whether these slightly larger fluctuations in case 3 lead to greater mixing is assessed using $\mathcal{P}(\xi)$ in figure 15. While the p.d.f.s at various axial locations look nearly identical, at locations in the transition region and downstream, i.e. $x/D \gtrsim 10$, the p.d.f. peaks are smaller and the profiles somewhat wider in case 3, a fact which indicates slightly larger scalar fluctuations and greater mixing than in case 5. This indicates that at same Z, larger velocity and thermodynamic fluctuations lead to enhanced mixing.

These results demonstrate that Z does not uniquely determine the flow dynamics because cases 3 and 5 that differ in p_∞ but have same Z exhibit small but noticeable differences in flow fluctuations and mixing. In particular, an increase in supercritical p_∞ at a fixed Z leads to reduced normalized velocity/pressure/density/scalar fluctuations, especially in the transition region. Therefore, the possible notion of performing experiments at a fixed Z and inferring from them information to another state having the same Z (i.e. same departure from perfect-gas behaviour) but larger p_∞, where experiments are more challenging, may be erroneous. Additionally, these results show that $p_\infty(\beta_T - 1/p_\infty)$ may also not be the non-dimensional thermodynamic parameter that completely determines flow behaviour, since, despite a large change in its value from case 3 to case 5 (approximately 30 % change), the results of the two cases are relatively close.

In thermodynamics, the law of corresponding states indicates that fluids at the same reduced temperature and reduced pressure have the same Z and, thus, exhibit similar departure from a perfect-gas behaviour. However, in fluid flows, dynamic effects characterized by the flow Mach number (here Ma_e) are also important, in addition to the thermodynamic effects characterized by Z, in determining the flow behaviour. Differences in Ma_e arise across cases 1–5 from the differences in the ambient speed of sound, and the effects of these differences are examined next.

4.3. *Effects of p_∞ and Z at a fixed jet-exit Mach number*

Comparisons between cases 1–4 in § 4.1 evaluated the effects of p_∞ and Z at a fixed jet-exit (inflow) bulk velocity, U_e. Different ambient thermodynamic conditions in cases 1–4 leads to different ambient speed of sound, c_∞, and hence different jet-exit (inflow) Mach number, Ma_e, values as shown in table 2. Thus, the results discussed so far do not distinguish between the influence of Mach number and the influence of

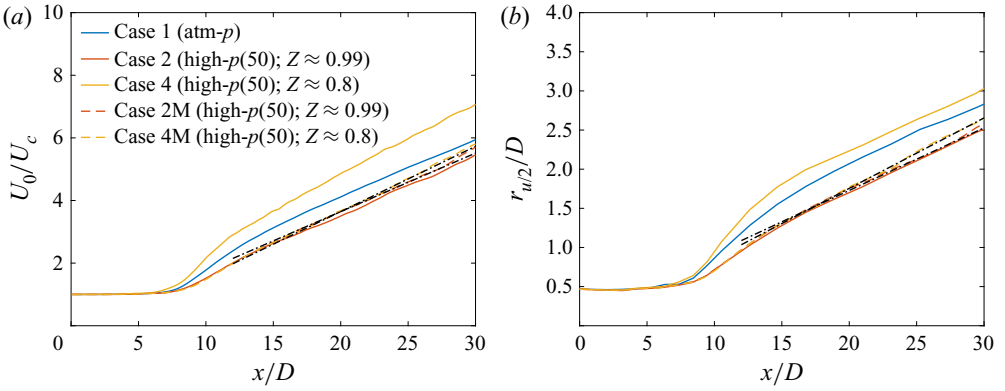

Figure 16. Fixed U_e vs fixed Ma_e cases: streamwise variation of (a) the inverse of centreline mean axial velocity (U_c) normalized by the jet-exit centreline velocity (U_0) and (b) the velocity half-radius ($r_{u/2}$) normalized by the jet diameter. The black dash-dotted lines in (a) are given by (C1) using $B_u = 5.35$, $x_{0u} = 0.5D$ for case 2M, and $B_u = 4.8$, $x_{0u} = 2.5D$ for cases 4M. The black dash-dotted lines in (b) are given by: $r_{u/2}/D = 0.08(x/D + 1.6)$ for case 2M, and $r_{u/2}/D = 0.09(x/D - 0.5)$ for case 4M. The self-similar profiles for cases 1, 2 and 4 are in figure 5 caption.

thermodynamic conditions. While a detailed assessment of the effects of Mach number is beyond the scope of this study, some conclusions may be extracted using results from cases 2M and 4M that have the same ambient thermodynamic conditions as cases 2 and 4, respectively, but where U_e is varied to yield a Ma_e of 0.6, which is the same value as that in case 1. The change in U_e from case 2, where $Ma_e = 0.58$, to case 2M is small, but from case 4, where $Ma_e = 0.82$, to case 4M is significant.

The centreline mean axial-velocity, plotted in figure 16(a), shows minor change from case 2 to 2M but notable differences between cases 4 and 4M. The small increase in Ma_e from case 2 to case 2M does not substantially affect the transition region behaviour but slightly increases the self-similar axial-velocity decay rate, $1/B_u$ in (C1), from 1/5.4 in case 2 to 1/5.35 in case 2M, whereas the decrease in Ma_e from case 4 to case 4M decreases the mean axial-velocity decay in the transition region as well as in the self-similar region, where $1/B_u$ reduces from 1/4.4 in case 4 to 1/4.8 in case 4M. The velocity half-radius, $r_{u/2}$, showing the jet spread in figure 16(b) depicts a similar behaviour, where minimal differences are observed between cases 2 and 2M, while the jet spread in case 4M is considerably reduced with respect to case 4. This shows that the unique behaviour of case 4, discussed in § 4.1, is a combined effect of its proximity to the Widom line and the inflow Mach number. This finding provides the motivation to examine the jet flow sensitivity to inflow condition in § 4.4.

To explore the differences observed in figure 16, the normalized velocity and pressure fluctuations among various cases are compared in figure 17. As noted in § 4.1.2, the magnitude of $u'_{c,rms}/U_c$ reflects the transfer of kinetic energy from the mean field to fluctuations and, consequently, its behaviour in figure 17(a) is correlated with the mean-flow behaviour in figure 16(a). Larger U_c decay rates in figure 16(a) occur in the regions of larger $u'_{c,rms}/U_c$ in figure 17(a). Furthermore, the increase in Ma_e from case 2 to case 2M enhances $p'_{c,rms}/p_c$, as seen in figure 17(b), whereas the decrease in Ma_e from case 4 to case 4M reduces it. At fixed $Ma_e = 0.6$, $p'_{c,rms}/p_c$ increases with decrease in Z from case 1 to case 2M to case 4M, indicating the role of Z at a fixed Ma_e. Thus, figure 17(b) in conjunction with figure 8(a) shows that, while at a fixed U_e, the comparative behaviour

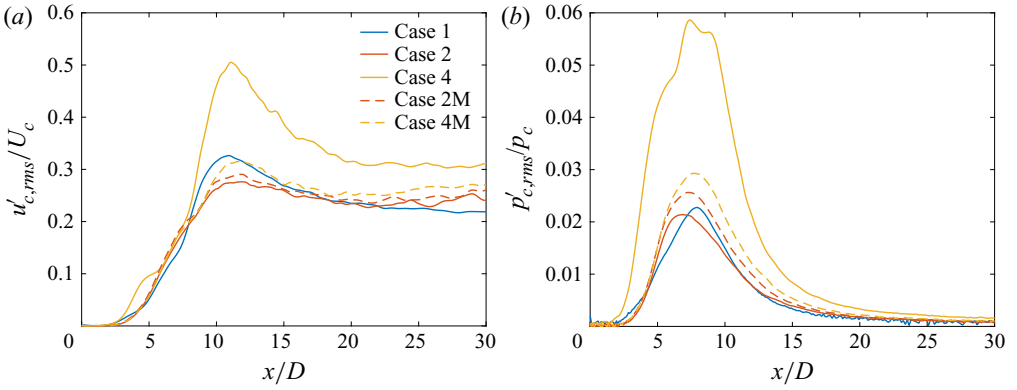

Figure 17. Fixed U_e vs fixed Ma_e cases: streamwise variation of (a) the centreline r.m.s. axial-velocity fluctuations ($u'_{c,rms}$) normalized by the centreline mean axial velocity (U_c) and (b) the centreline r.m.s. pressure fluctuations ($p'_{c,rms}$) normalized by the centreline mean pressure (p_c).

of $p'_{c,rms}/p_c$ is correlated with the value of $p_\infty(\beta_T - 1/p_\infty)$ in table 3, this may not be the case at a fixed Ma_e.

Examination of normalized fluctuating pressure–velocity correlation and third-order velocity moments (not presented here for brevity) showed that their behaviour is correlated with the mean and fluctuating axial-velocity behaviour in figures 16(a) and 17(a), respectively. This feature of the flow is further investigated in the next section to explain the physical mechanism by which thermodynamic and inflow conditions influence the jet-flow dynamics and mixing.

4.4. *Inflow effects*

The influence of inflow conditions on near- and far-field jet-flow statistics at atmospheric conditions has been a subject of numerous investigations, e.g. Husain & Hussain (1979), Richards & Pitts (1993), Boersma *et al.* (1998), Mi *et al.* (2001) and Xu & Antonia (2002). Several studies have questioned the classical self-similarity hypothesis (Townsend 1980) that the asymptotic state of the jet flow depends only on the rate at which momentum is added and is independent of the inflow conditions. Those studies support the analytical result of George (1989), who suggested that the flow can asymptote to different self-similar states determined by the inflow condition. It is thus pertinent to use the two inflow conditions described in § 3.2.2 to examine the uniqueness of the self-similar state at near-atmospheric p_∞. In contrast to past investigations in which measurements were obtained of either the velocity or the passive scalar field, here, the inflow effects on the velocity and the scalar field are simultaneously examined, first at perfect-gas conditions in § 4.4.1, and then at high-p conditions in § 4.4.2.

4.4.1. *Inflow effects at perfect-gas condition: comparisons between cases 1 and 1T*

For the laminar inflow, which has a top-hat jet-exit mean velocity profile (3.1), the jet-exit bulk velocity is approximately U_e, and U_e is equal to the jet-exit centreline velocity, U_0. However, for the turbulent inflow, which has a parabolic jet-exit mean velocity profile, the jet-exit bulk velocity, U_e, is smaller than U_0. The present study uses the same U_e for all cases, except cases 2M and 4M. As a result, U_0 is different for the laminar- and turbulent-inflow cases.

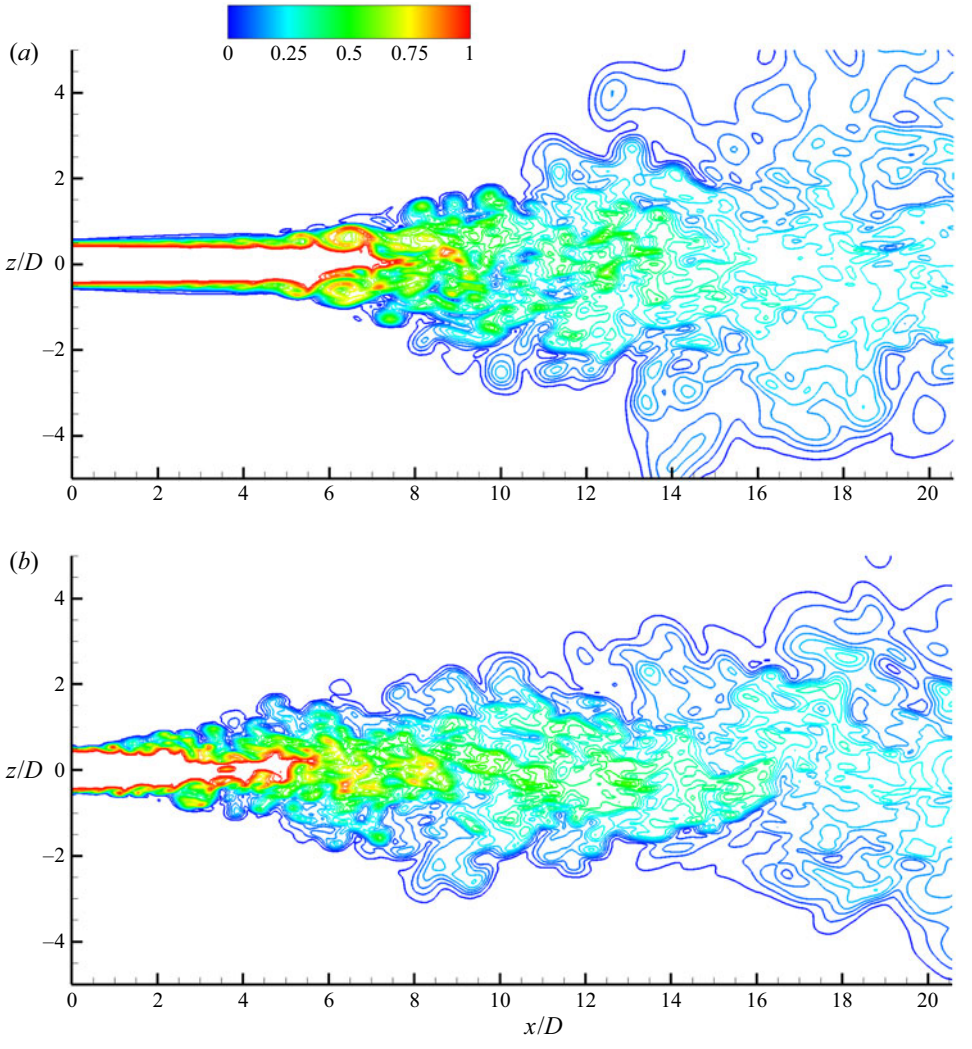

Figure 18. Near-field instantaneous scalar contours at $tU_e/D \approx 3500$ from (*a*) case 1 and (*b*) case 1T showing the mixed-fluid concentration. The contour lines show 24 levels in the range $0.02 \leq \xi \leq 0.98$. The legend is the same for both plots.

Figure 18 illustrates the near-field scalar contours from cases 1 and 1T at $tU_e/D \approx 3500$. The rendered contour lines show the mixed fluid, defined as $0.02 \leq \xi \leq 0.98$. Evidently, the near-field flow features are considerably different for the two jets. The instabilities in the annular shear layer that trigger vortex roll-ups appear at larger axial distance in the jet from the laminar inflow (case 1) than those in the jet from the pseudo-turbulent inflow (case 1T). The inflow disturbances in case 1T, modelling pipe-flow turbulence, are broadband and higher in magnitude, thus triggering small-scale turbulence that promote axial shear-layer growth immediately downstream of the jet exit. In contrast, the laminar inflow has small random disturbances superimposed over the top-hat velocity profile that trigger the natural instability frequency (Ho & Nosseir 1981) and dominant vortical structures/roll-up around $x/D \approx 5$. The larger axial distance required for the natural instability to take effect in case 1 leads to a longer potential core than in

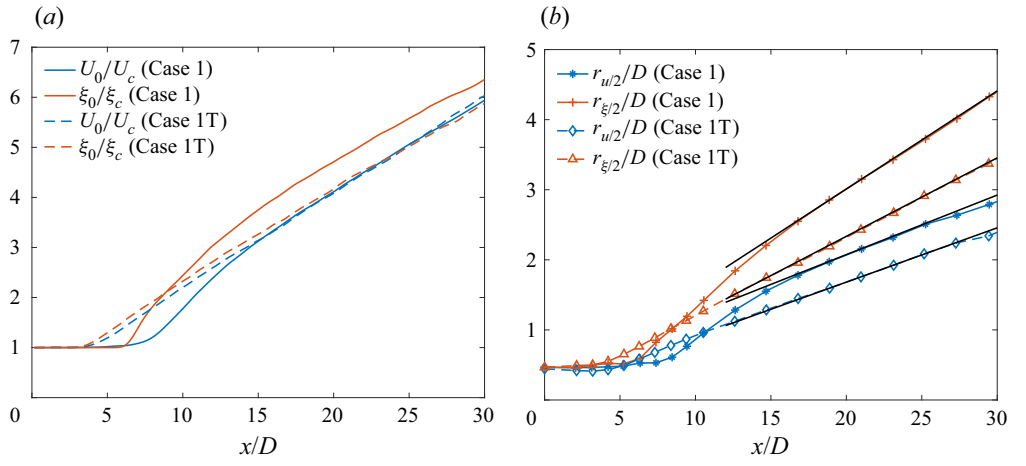

Figure 19. Case 1 and 1T comparisons: streamwise variation of the (*a*) inverse of centreline mean axial velocity (U_c) and scalar concentration (ξ_c) normalized by the jet-exit centreline mean values and (*b*) normalized velocity and scalar half-radius, denoted by $r_{u/2}/D$ and $r_{\xi/2}/D$, respectively. The linear profile downstream of $x/D \approx 15$ in (*a*) can be described by (C1) using $B_u = 5.5$ ($x_{0u} = -2.4D$) and $B_\xi = 5.75$ ($x_{0\xi} = -3.5D$) for case 1T, whereas $B_u = 5.5$ ($x_{0u} = -2.4D$) and $B_\xi = 5.7$ ($x_{0\xi} = -6.8D$) for case 1. The black solid lines in (*b*) are given by: $r_{u/2}/D = 0.085(x/D + 4.4)$ and $r_{\xi/2}/D = 0.14(x/D + 1.5)$ for case 1, and $r_{u/2}/D = 0.078(x/D + 1.7)$ and $r_{\xi/2}/D = 0.11(x/D + 0.85)$ for case 1T.

case 1T. However, once the instabilities take effect in case 1, at $x/D \approx 5$, dominant vortical structures close the potential core over a short distance, i.e. around $x/D \approx 8$. In comparison, in case 1T, the broadband small-scale turbulence triggered immediately downstream of the jet exit closes the potential core around $x/D \approx 6$. Downstream of the potential core collapse, an abrupt increase in the jet width is observed in case 1, while the jet grows gradually in case 1T.

The above-discussed qualitative differences are now quantified using various velocity and scalar statistics.

4.4.1.1. Velocity and scalar statistics, and self-similarity A comparison of U_c and ξ_c axial decay between case 1 and case 1T jets is presented in figure 19(*a*). The shorter potential core length of case 1T leads to velocity and scalar decay beginning upstream of that in case 1. The difference between the axial locations where the velocity and scalar begin to decay is noticeable for case 1, while it is relatively small for case 1T, thus indicating a tighter coupling of the dynamics and molecular mixing in case 1T. The upstream decay of the scalar, with respect to velocity, in the laminar-inflow jet (case 1) is consistent with the observation of Lubbers, Brethouwer & Boersma (2001, figure 6) for a passive scalar diffusing at unity Schmidt number. Also noticeable in the case 1 results is a transition or development region, $7 \lesssim x/D \lesssim 15$, where the velocity and scalar decay rates are larger than in the asymptotic state reached further downstream. The case 1T results do not show a similarly distinctive transition region, and the velocity and scalar decay rates remain approximately the same downstream of the potential core closure. Downstream of $x/D \approx 15$, the velocity and scalar decay rates are similar for cases 1 and 1T.

The velocity and scalar half-radius for cases 1 and 1T are compared in figure 19(*b*). The case 1 jet spreads at a faster rate than case 1T, consistent with the experimental observations of Xu & Antonia (2002) and Mi *et al.* (2001). The decrease in velocity

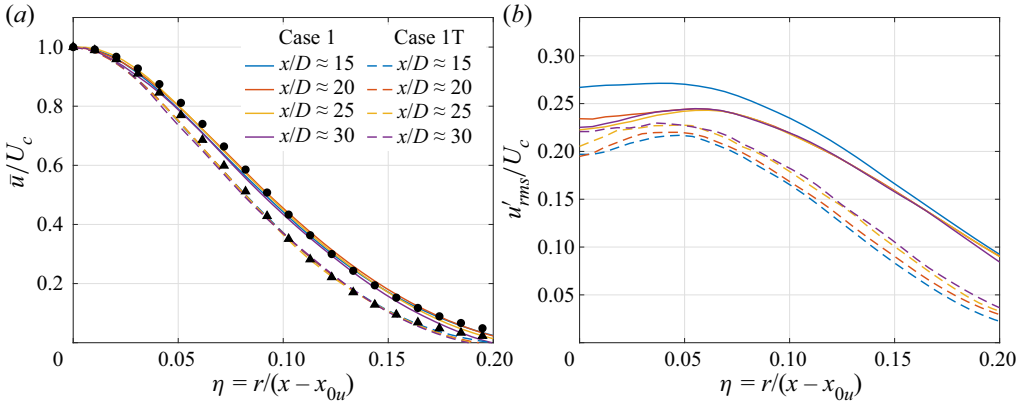

Figure 20. case 1 and 1T comparisons: radial profiles of (a) mean axial velocity ($\bar{u}$) and (b) r.m.s. axial-velocity fluctuations (u'_{rms}) normalized by the centreline mean velocity (U_c) at various axial locations. The markers • and ▲ in (a) show $f(\eta)$ of (4.2a,b) using $A_u = 79.5$ and 99, respectively. The legend is the same for both plots.

half-radius spreading rate from 0.085 (case 1) to 0.078 (case 1T) is consistent with the observations of Xu & Antonia (2002), where a decrease in spreading rate from 0.095 for the jet issuing from a smooth contraction nozzle to 0.086 for the jet from a pipe nozzle was reported. The spreading rates of 0.14 and 0.11 based on the scalar half-radius for case 1 and case 1T, respectively, are larger than the values of 0.11 and 0.102 reported by Mi *et al.* (2001) for their temperature scalar field from smooth contraction nozzle and pipe jet, respectively, but comparable to the values of 0.13 and 0.11 deduced from the results of Richards & Pitts (1993) for their mass-fraction scalar field from smooth contraction nozzle and pipe jet, respectively. The profiles in figure 19 also show that the velocity and scalar mean fields attain self-similarity, i.e. their centreline values decay linearly and the half-radius spreads linearly, at smaller axial distance in case 1T than in case 1. In the self-similar region, the U_c and ξ_c decay rates of cases 1 and 1T are comparable, while the half-radius spreading rates differ. The non-dimensional U_0/U_c have similar values for cases 1 and 1T in the self-similar region, but since U_0 is different for case 1 and case 1T, U_c differs accordingly. The results of mean velocity/scalar centreline behaviour and jet spread suggest that these quantities strongly depend on the inflow condition, both in the near field and the self-similar region, thus highlighting the importance of reporting inflow conditions in experimental studies if their data have to be used for model validation.

To further examine the differences between cases 1 and 1T, and the self-similar state attained in these flows, the radial variation of axial velocity and its fluctuation are documented in figure 20. Examination of figure 20(a) shows that the mean axial velocity attains self-similarity as near stream as $x/D \approx 15$ for both cases 1 and 1T, however, the self-similar profiles are different. The solid markers in figure 20(a) show the $f(\eta)$ profiles of (4.2a,b) using $A_u = 79.5$ (circles) and 99 (triangles). These values are comparable to the values of 76.5 and 90.2 reported by Xu & Antonia (2002) for jets from a smooth contraction and pipe nozzle, respectively. Radial profiles of u'_{rms}/U_c from cases 1 and 1T are compared in figure 20(b). Here, u'_{rms}/U_c attains self-similarity around $x/D \approx 25$, a location which is further downstream than for $\bar{u}/U_c$, in both cases 1 and 1T; minor differences remain near the centreline between the profiles at $x/D \approx 25$ and 30. The u'_{rms}/U_c values from case 1T are smaller than those from case 1 at all shown axial locations, especially away from the centreline, consistent with the experimental

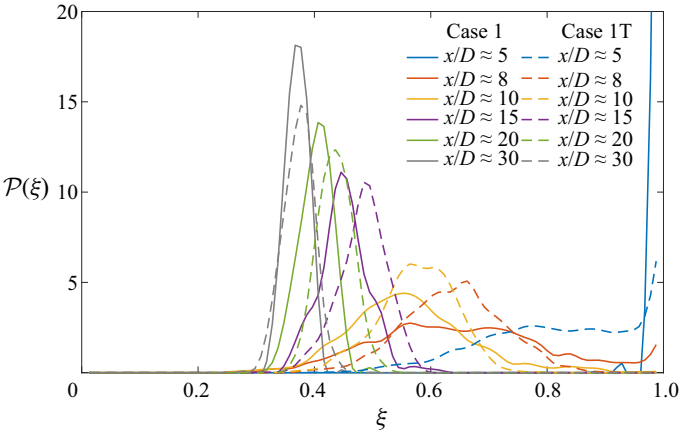

Figure 21. Case 1 and 1T comparisons: scalar p.d.f., $\mathcal{P}(\xi)$, at various centreline axial locations.

observations of Xu & Antonia (2002) with laminar/turbulent inflow. Figure 20(*b*) also shows that, for case 1, u'_{rms}/U_c in the near field ($x/D \approx 15$) is larger than that in the self-similar regime, especially in the radial vicinity of the centreline, while for case 1T, the near-field ($x/D \approx 15$) values are smaller than that in the self-similar regime. The u'_{rms}/U_c values in the near field are, therefore, considerably larger with laminar inflow than with turbulent inflow. The behaviour of other Reynolds stress components, v'_{rms}/U_c, w'_{rms}/U_c and $\overline{u'v'}/U_c^2$, not shown here for brevity, is similar to that of u'_{rms}/U_c in that all of them show self-similarity around $x/D \approx 25$ but the self-similar profiles depend on the inflow condition. Moreover, their near-field values are much higher in case 1 than in case 1T, as for u'_{rms}/U_c. Thus, similar to the mean quantities in figure 19, the Reynolds stress components also show strong sensitivity to the inflow condition.

4.4.1.2. Passive scalar mixing To examine the differences in scalar mixing between cases 1 and 1T, figure 21 compares the scalar p.d.f., $\mathcal{P}(\xi)$, at various locations along the jet centreline. Significant differences are observed in the near-field p.d.f. profiles, i.e. for $x/D \lesssim 15$. The locations $x/D \approx 5$ and 8 are approximately the centreline location of maximum (non-dimensionalized) scalar fluctuations for case 1T and case 1, respectively, as shown in figure 22. Since the jet-exit centreline mean scalar value is $\xi_0 = 1$ for all cases, normalization of $\xi'_{c,rms}$ with ξ_0 in figure 22 allows a comparison of the absolute fluctuation magnitude between case 1 and case 1T. The value of $\xi'_{c,rms}/\xi_0$ peaks when the potential core closes and then decreases with axial distance for each case. In contrast, the local normalization with ξ_c asymptotes to a constant value at large axial distances. The value of $\xi'_{c,rms}/\xi_c$ exhibits a prominent hump, or a local maximum, in the near field for case 1, consistent with the experimental observations in jets from a smooth contraction nozzle (Mi *et al.* 2001).

Comparison of p.d.f. profiles at $x/D \approx 5$ in figure 21 between case 1 and 1T shows pure jet fluid ($\xi = 1$) for case 1, but mixed fluid with scalar concentrations ranging from 0.5 to 1 for case 1T, as expected, since the potential core closes before $x/D \approx 5$ in case 1T, but after $x/D \approx 5$ in case 1. At $x/D \approx 8$ and 10, the p.d.f. profiles for case 1 exhibit a wider spread compared with that for case 1T. Stronger large-scale vortical structures in the near field (around $x/D \approx 8$) in case 1, as seen in figure 18(*a*), entrain ambient fluid deep into the jet

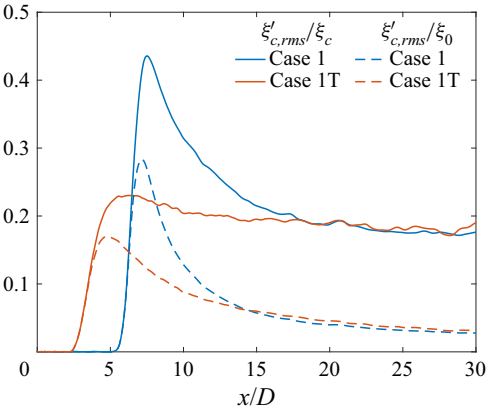

Figure 22. Case 1 and 1T comparisons: streamwise variation of the centreline r.m.s. scalar fluctuation ($\xi'_{c,rms}$) normalized by the centreline mean scalar value (ξ_c) and the jet-exit centreline mean scalar value (ξ_0).

core, resulting in larger scalar fluctuations (see figure 22) and a wider distribution of scalar concentrations at the centreline. In contrast, mixing in case 1T occurs through small-scale structures resulting in weaker entrainment of ambient fluid and smaller scalar fluctuations. The p.d.f. profiles for case 1T at $x/D \approx 8$ and 10 are, therefore, narrower with higher peaks. Larger scalar fluctuations in the transition region ($7 \lesssim x/D \lesssim 15$) of case 1, resulting from large-scale organized structures, cause greater mixing and, consequently, steeper decay of the centreline mean scalar concentration (ξ_c), as observed in figure 19(a). The centreline mean scalar concentration, indicated by the scalar value at peaks of the p.d.f. profiles in figure 21, is smaller (or closer to the ambient scalar value of 0) for case 1 downstream of $x/D \approx 10$. The difference between the scalar mean values from the two cases diminishes with axial distance. With increase in axial distance, the jet width (see figure 19b) increases and the absolute centreline scalar fluctuation (see figure 22) diminishes. As a result, the spread of the scalar p.d.f. profile declines and the peaks become sharper downstream of $x/D \approx 10$.

4.4.1.3. Summary To conclude, both velocity and scalar statistics show sensitivity to the inflow condition. In the near field, the jet flow from laminar inflow (case 1) is characterized by strong vortical structures leading to larger velocity/scalar fluctuations and jet spreading rate in the transition region than case 1T. Further downstream, self-similarity is observed in velocity/scalar mean and fluctuations, but the self-similar profiles differ with the inflow, supporting the argument that they may not be universal. This indicates that a quantitative knowledge of the experimental inflow conditions is important in validating simulation results against experiments. Whether these conclusions hold at high pressures is examined next.

4.4.2. *Inflow effects at high pressure: comparisons between cases 1/1T, 2/2T and 4/4T*
A crucial observation from § 4.1, where the influence of p_∞ and Z on the jet-flow dynamics and mixing was examined, is that $p'_{c,rms}/p_c$ decreases with increase in p_∞ from 1 bar (case 1) to 50 bar (case 2), and increases with decrease in Z from 0.99 (case 2) to 0.8 (case 4), as shown in figure 8(a); the velocity/scalar mean and fluctuations (figures 5a, 6 and 12), however, follow the behaviour of the normalized t.k.e. diffusive fluxes (and not

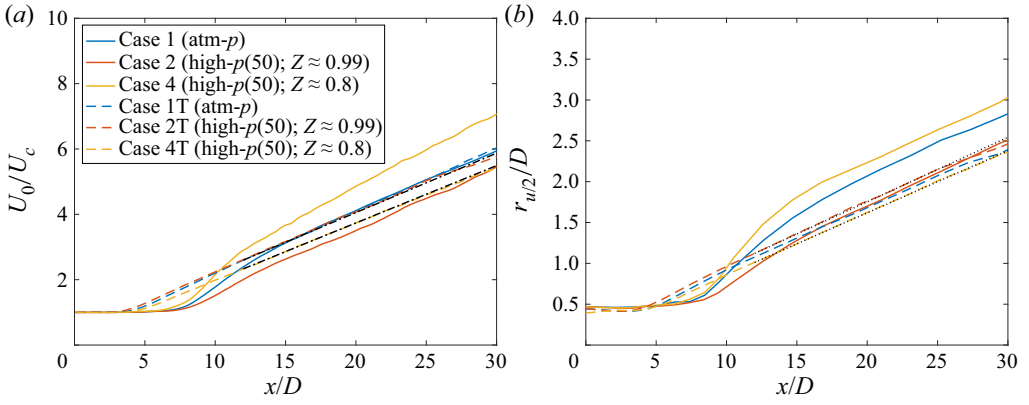

Figure 23. Comparisons of different inflow cases: streamwise variation of the (*a*) inverse of centreline mean velocity (U_c) normalized by the jet-exit centreline velocity (U_0) and (b) velocity half-radius ($r_{u/2}$). The black dash-dotted lines in (*a*) are given by (C1) using $B_u = 5.5, x_{0u} = -2.3D$ for case 2T and $B_u = 5.7, x_{0u} = -1.3D$ for case 4T. Details of lines showing the self-similar profile of (C1) for cases 1, 2, 4 and 1T are presented in figures 5 and 19. The black dotted lines in (*b*) are given by $r_{u/2}/D = 0.079(x/D + 2.2)$ for case 2T and $r_{u/2}/D = 0.076(x/D + 1.3)$ for case 4T.

of $p'_{c,rms}/p_c$), e.g. $(\overline{p'u'}/\bar{\rho})/U_c^3$ and $\overline{u'^3}/U_c^3$ shown in figures 8(*b*) and 8(*c*), respectively. Those observations are for laminar-inflow jets, and the validity of those observations is here examined in pseudo-turbulent inflow jets (inflow details in § 3.2.2).

To examine the effects of inflow variation at supercritical p_∞, case 2 results are here compared with case 2T, and case 4 with case 4T. These results in conjunction with those of § 4.4.1 provide an enlarged understanding of the effect of inflow conditions at different p_∞ and Z.

4.4.2.1. Mean axial velocity and spreading rate Figure 23(*a*) illustrates the centreline variation of mean axial velocity in cases 1/1T, 2/2T and 4/4T. In concurrence with the observation for case 1T against case 1, discussed in § 4.4.1, the pseudo-turbulent-inflow cases at supercritical pressure (cases 2T and 4T) also exhibit a shorter potential core than their laminar-inflow counterparts (cases 2 and 4). As a result, the axial location where the mean velocity decay begins for cases 1T, 2T and 4T is upstream of the corresponding location for cases 1, 2 and 4. The laminar-inflow cases show a distinct transition region ($7 \lesssim x/D \lesssim 15$) with larger mean velocity decay rate than that further downstream in their self-similar region. A similar change in decay rate (equal to the slope of the plot lines) does not occur in cases 1T, 2T and 4T, where the slopes remain approximately the same downstream of the potential core closure. The linear decay rate in the self-similar region is described by $1/B_u$, defined by (C1). The B_u values for various cases are included in the caption of figure 23(*a*). For cases 1 and 1T, the decay rates are the same; between cases 2 and 2T, the decay rate is slightly larger in the laminar-inflow jet (case 2), and between cases 4 and 4T, the decay rate is significantly larger in the laminar-inflow jet (case 4).

To investigate the differences in jet spread, $r_{u/2}$ from different inflow cases are compared in figure 23(*b*). As expected from smaller potential core length in the pseudo-turbulent-inflow cases, $r_{u/2}$ growth in cases 1T, 2T and 4T begins upstream of that in cases 1, 2 and 4. Immediately downstream of the potential core closure, $r_{u/2}$ in laminar inflow cases (cases 1, 2 and 4) grows at a relatively faster rate than in cases 1T, 2T and 4T. The linear $r_{u/2}$ profiles in the self-similar region of cases 1, 2, 4 and 1T are given in

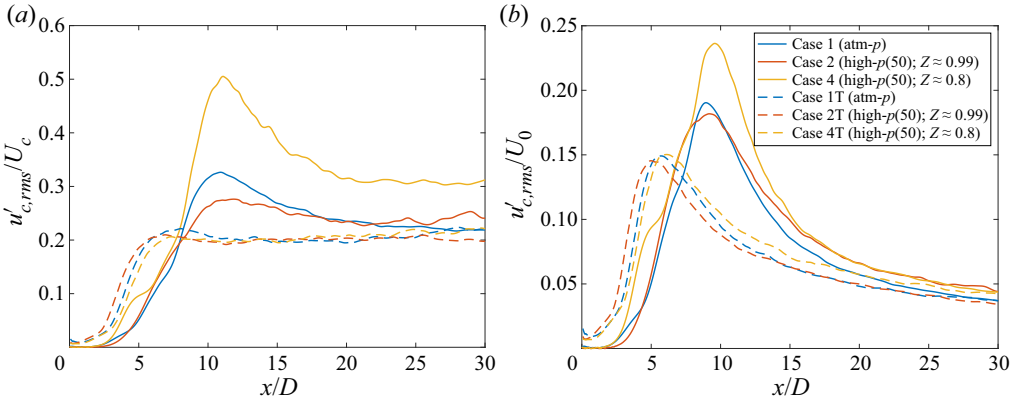

Figure 24. Comparisons of different inflow cases: streamwise variation of the (*a*) the centreline r.m.s. axial-velocity fluctuations ($u'_{c,rms}$) normalized by the centreline mean axial velocity (U_c), (*b*) $u'_{c,rms}$ normalized by the jet-exit centreline mean axial velocity (U_0). The legend is the same for both plots.

figures 5 and 19. The profiles for cases 2T and 4T are listed in the figure caption. The inflow change from laminar to pseudo-turbulent reduces the spreading rate at atmospheric as well as supercritical conditions. The change is significant at atmospheric conditions (from 0.085 in case 1 to 0.078 in case 1T) and relatively small for supercritical cases (from 0.0805 in case 2 to 0.079 in case 2T and 0.077 in case 4 to 0.076 in case 4T). A noticeable feature in the self-similar region of figure 23(*b*) is the difference in $r_{u/2}$ among various cases for the two inflows; for laminar inflow, $r_{u/2}$ decreases from case 1 to case 2 and increases from case 2 to case 4, whereas the differences are comparatively minimal between cases 1T, 2T and 4T. In fact, $r_{u/2}$ in cases 1T and 2T are slightly larger than that in case 4T.

The decay in mean velocity occurs in part due to the transfer of kinetic energy from the mean field to fluctuations, as discussed in § 4.1.1. To determine if the differences observed here in the mean velocity are consistent with the variations in velocity fluctuations, they are examined next.

4.4.2.2. Velocity fluctuations and self-similarity To understand the differences observed in figure 23, the centreline variation of axial-velocity fluctuations is compared for various inflow cases in figure 24. The value of $u'_{c,rms}/U_c$, presented in figure 24(*a*), reflects the local mean energy transfer to fluctuations. As discussed in § 4.1, higher $u'_{c,rms}/U_c$ implies larger mean axial-velocity decay rate or higher slope of the line in figure 23(*a*). In the transition region, the laminar inflow cases exhibit significant differences with increase in p_∞ (from case 1 to case 2) as well as with decrease in Z (from case 2 to case 4). In contrast, the differences are minimal between cases 1T, 2T and 4T. In the transition region of these cases ($3 \lesssim x/D \lesssim 8$), $u'_{c,rms}/U_c$ in case 4T is slightly smaller than that in cases 1T and 2T. Accordingly, the mean axial-velocity decay rate is smaller for case 4T in the transition region, see figure 23(*a*). The difference between the asymptotic value attained by $u'_{c,rms}/U_c$ is small between cases 1 and 1T, but significant at supercritical p_∞ between cases 2 and 2T and cases 4 and 4T. The difference is particularly large between cases 4 and 4T, consistent with the large difference in their U_c decay rates in the self-similar region of figure 23. Thus, the variation in axial-velocity fluctuations consistently represents the transfer of mean kinetic energy to t.k.e.

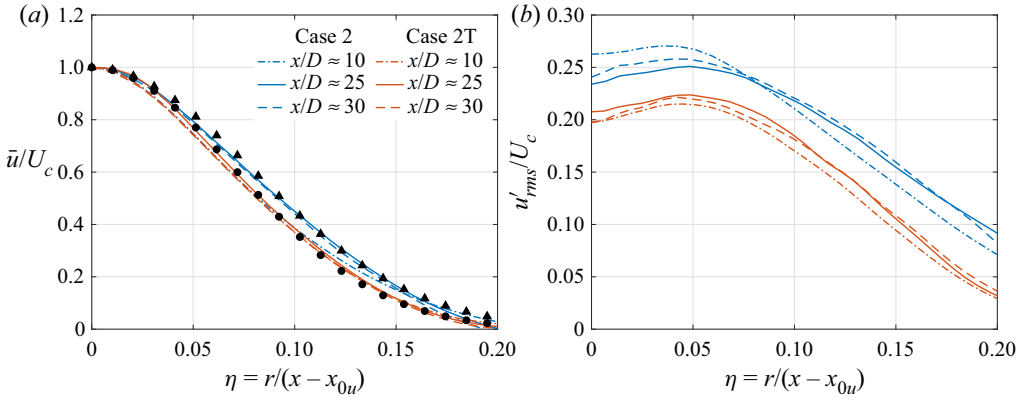

Figure 25. Case 2 and 2T comparisons: radial profiles of (a) mean axial velocity ($\bar{u}$) normalized by the centreline mean axial velocity (U_c), (b) r.m.s. axial-velocity fluctuations (u'_{rms}) normalized by the centreline mean axial velocity at various axial locations. The markers ▲ and • in (a) show $f(\eta)$ of (4.2a,b) using $A_u = 79.5$ and 99.2, respectively. The legend is the same for both plots.

Normalizing $u'_{c,rms}$ with U_0, as presented in figure 24(b), enables a comparison of the absolute fluctuation magnitude for each inflow (U_0 differs for the two inflows, as discussed in § 4.4.1). In figure 24(b), $u'_{c,rms}/U_0$ decreases with axial distance, unlike $u'_{c,rms}/U_c$ in figure 24(a) that asymptotes to a constant value. The peak of $u'_{c,rms}/U_0$, attained in the transition region, decreases with increasing p_∞ from 1 bar to 50 bar and increases with decreasing Z from 0.99 to 0.8 for each inflow. The $u'_{c,rms}/U_c$ and $u'_{c,rms}/U_0$ magnitudes and their differences are larger in the laminar-inflow cases, especially in the transition region of the flow, showing that the effect of p_∞ and Z depends strongly on the inflow, in addition to the ambient thermodynamic state characterized by $p_\infty(\beta_T - 1/p_\infty)$.

To examine self-similarity in the flow, the radial variations of mean axial velocity and r.m.s. axial-velocity fluctuations at three axial locations are compared between cases 2 and 2T and cases 4 and 4T in figures 25 and 26, respectively. The axial location $x/D \approx 10$ lies around the jet transition region in both inflow cases, whereas the profiles at $x/D \approx 25$ and 30 help assess self-similarity. Figure 25(a) shows that $\bar{u}/U_c$ attains self-similarity upstream of $x/D \approx 25$ in both cases (2 and 2T); however, the self-similar profile is different, as shown by the least-squares fits of the Gaussian distribution, $f(\eta)$ of (4.2a,b), to $x/D \approx 30$ profiles, depicted as solid black markers in figure 25(a). The u'_{rms}/U_c profiles at $x/D \approx 25$ and 30 in figure 25(b) exhibit only minor differences in both cases 2 and 2T, suggesting that u'_{rms}/U_c is self-similar around $x/D \approx 25$. The value of u'_{rms}/U_c is considerably larger in the laminar-inflow case (case 2) at all η locations, consistent with the observations at atmospheric p_∞ between cases 1 and 1T in figure 20(b). Similarly, v'_{rms}/U_c, w'_{rms}/U_c, and $\overline{u'v'}/U_c^2$ (not shown here for brevity) are also larger in case 2 than case 2T and show self-similarity around $x/D \approx 25$.

The values of $\bar{u}/U_c$ from cases 4 and 4T are compared in figure 26(a). As in figures 20(a) and 25(a) for cases 1/1T and 2/2T, the self-similar profiles are different for the two inflows, and this difference is amplified with respect to cases 2/2T as the solid markers in figure 26(a) that display the Gaussian distribution, $f(\eta)$ of (4.2a,b), show. The value of u'_{rms}/U_c illustrated in figure 26(b) shows self-similarity around $x/D \approx 25$ for both cases (4 and 4T) and larger magnitude in the laminar-inflow case (case 4). The values of v'_{rms}/U_c, w'_{rms}/U_c and $\overline{u'v'}/U_c^2$ show similar behaviour, and are not shown here for brevity.

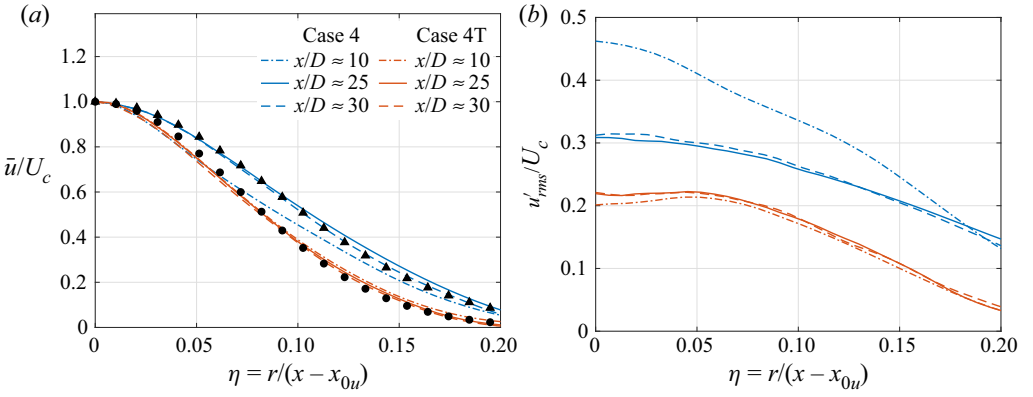

Figure 26. Case 4 and 4T comparisons: radial profiles of (a) mean axial velocity ($\bar{u}$) normalized by the centreline mean axial velocity (U_c), (b) r.m.s. axial-velocity fluctuations (u'_{rms}) normalized by the centreline mean axial-velocity at various axial locations. The markers ▲ and ● in (a) show $f(\eta)$ of (4.2a,b) using $A_u = 64.4$ and 99.2, respectively. The legend is the same for all plots.

The spatial variation of thermodynamic (pressure/density) fluctuations and their correlation with velocity fluctuations, that determines the transport terms in the t.k.e. equation, were used to explain the jet-flow dynamics for various p_∞ and Z in § 4.1.3 and, therefore, these quantities are examined next to determine if they can explain the differences with inflow condition discussed above.

4.4.2.3. Pressure and density fluctuations, pressure-velocity correlation and third-order velocity moments Centreline variations of $p'_{c,rms}/p_c$ and $\rho'_{c,rms}/\rho_c$ are presented in figures 27(a) and 27(b), respectively. The values of $p'_{c,rms}/p_c$ and $\rho'_{c,rms}/\rho_c$ are negligible at jet exit in laminar-inflow cases but have significant magnitude in pseudo-turbulent-inflow cases, where it decreases with axial distance until the potential core closes and increases in the transition region. Variations of $p'_{c,rms}/p_c$ and $\rho'_{c,rms}/\rho_c$ with p_∞ and Z are similar for the two inflows. $p'_{c,rms}/p_c$ and $\rho'_{c,rms}/\rho_c$ are larger in case 4 than in cases 1 and 2 and, similarly, they are higher in case 4T than in cases 1T and 2T. With increase in p_∞ from 1 bar (cases 1 and 1T) to 50 bar (cases 2 and 2T), the peak value of $p'_{c,rms}/p_c$ and $\rho'_{c,rms}/\rho_c$ in the transition region decreases by a small value. The differences diminish downstream in the self-similar region. The values of $p'_{c,rms}/p_c$ and $\rho'_{c,rms}/\rho_c$ increase with decrease in Z from 0.99 (cases 2 and 2T) to 0.8 (cases 4 and 4T) for both inflows, especially in the transition region of the flow. On the other hand, $u'_{c,rms}/U_c$, presented in figure 24(a), increases with decreasing Z for laminar inflow but remains approximately the same in pseudo-turbulent-inflow cases. In fact, in the transition region, $u'_{c,rms}/U_c$ is slightly smaller in case 4T than case 2T, while it is larger in case 4 than case 2. This anomaly with inflow change leads to contrasting mean flow behaviour, observed in figure 23 in the transition region, where the mean axial-velocity decay and jet half-radius increases from case 2 to case 4 but decreases from case 2T to case 4T.

To investigate this anomaly, the centreline variation of t.k.e. diffusion fluxes from turbulent transport is compared in figures 28 and 29. Figure 28 compares $(\overline{p'u'}/\bar{\rho})/U_c^3$, which determines the t.k.e. diffusion due to pressure fluctuation transport. To highlight the differences among pseudo-turbulent-inflow cases with suitable y-axis scale, figure 28(b) shows only the results from cases 1T, 2T and 4T. In the transition region, the absolute

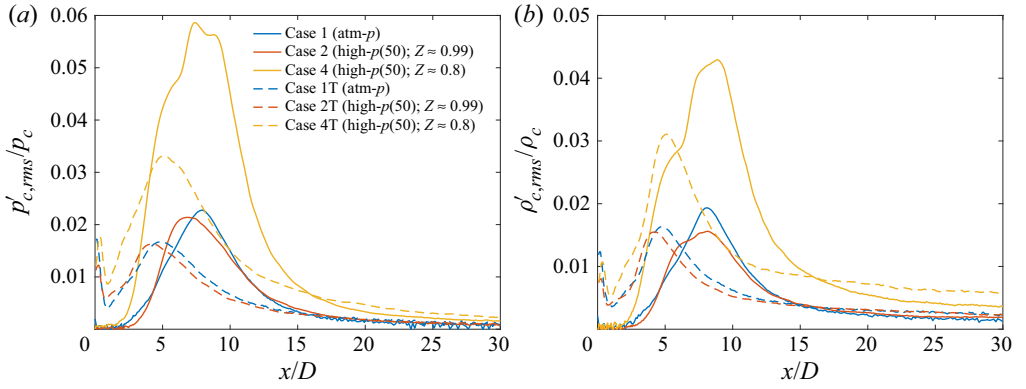

Figure 27. Comparisons of different inflow cases: streamwise variation of the (*a*) the centreline r.m.s. pressure ($p'_{c,rms}$) normalized by the centreline mean pressure (p_c) and (*b*) the centreline r.m.s. density fluctuations ($\rho'_{c,rms}$) normalized by the centreline mean density (ρ_c). The legend is the same for both plots.

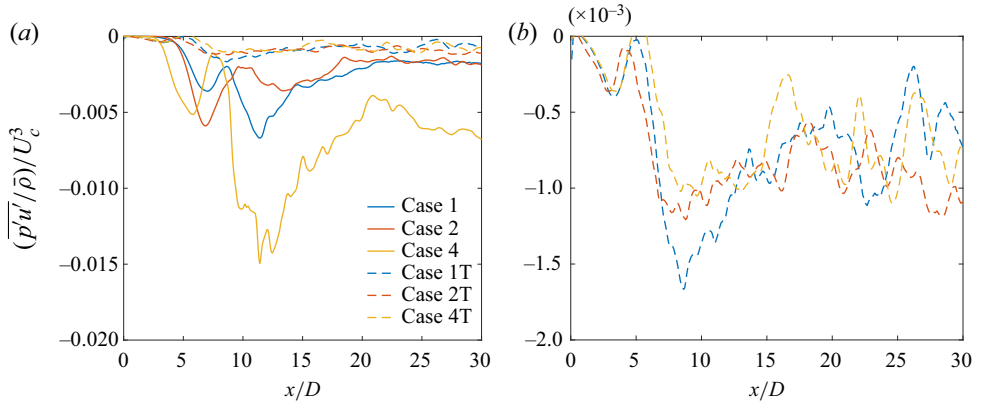

Figure 28. Comparisons of different inflow cases: streamwise variation of the normalized pressure–axial-velocity correlation for (*a*) the laminar and pseudo-turbulent-inflow cases, and (*b*) only the pseudo-turbulent-inflow cases. Note the difference between *y*-axis scales of (*a*,*b*).

magnitude of $(\overline{p'u'}/\bar{\rho})/U_c^3$ increases from case 2 to case 4 but decreases from case 2T to 4T, indicating that the t.k.e. diffusion due to pressure fluctuation transport increases in the laminar inflow jet but decreases in the pseudo-turbulent inflow-jet. Further downstream, the differences are significant between cases 2 and 4, but minimal between cases 2T and 4T, implying that the effects of Z (or the effects of ambient thermodynamic conditions closer to the Widom line) are enhanced in the laminar-inflow jets.

The value of $\overline{u'^3}/U_c^3$, which determines the t.k.e. diffusion flux from turbulent transport of $\overline{u'^2}$, is compared between cases 1/1T, 2/2T and 4/4T in figure 29(*a*) and among cases 1T/2T/4T in figure 29(*b*). While there are significant differences in $\overline{u'^3}/U_c^3$ profiles of cases 1, 2 and 4, the differences are, again, minimal among cases 1T, 2T and 4T. Thus, both $(\overline{p'u'}/\bar{\rho})/U_c^3$ and $\overline{u'^3}/U_c^3$ show greater sensitivity to the ambient thermodynamic state, characterized by $p_\infty(\beta_T - 1/p_\infty)$, in the laminar-inflow jets, and their variation in figures 28 and 29 for various cases agrees well with the behaviour of $u'_{c,rms}/U_c$ in figure 24(*a*) and the mean-flow metrics in figure 23.

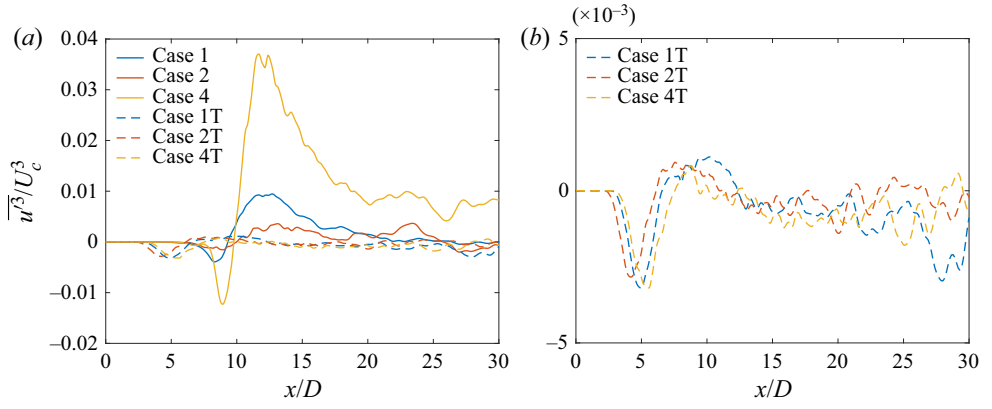

Figure 29. Comparisons of different inflow cases: streamwise variation of $\overline{u'^3}/U_c^3$ for (*a*) the laminar and pseudo-turbulent-inflow cases, and (*b*) only the pseudo-turbulent-inflow cases. Note the difference between *y*-axis scales of (*a*,*b*).

4.4.2.4. Passive scalar mixing To examine passive scalar mixing with inflow change at high pressure, the scalar p.d.f. is depicted in figure 30; cases 2 and 2T are compared at various x/D in figure 30(*a*) and, similarly, cases 4 and 4T are compared in figure 30(*b*). As observed at atmospheric p_∞ (figure 21), the p.d.f. at $x/D \approx 5$ in figure 30(*a*) shows pure jet fluid in the laminar-inflow case (case 2), whereas mixed fluid in the case of pseudo-turbulent inflow (case 2T). At $x/D \approx 8$ and 10, the p.d.f. has a wider distribution in case 2 owing to stronger large-scale vortical structures that yield larger normalized scalar fluctuations, $\xi'_{c,rms}/\xi_0$, as shown in figure 31(*b*). Further downstream, the p.d.f. profiles show minor differences, consistent with the scalar mean and fluctuation behaviour observed in figure 31. Thus, at supercritical p_∞, but with ambient conditions far from the Widom line (with near-unity Z), the influence of the inflow on scalar mixing is restricted to the near field. Figure 30(*b*) shows that the situation changes when the ambient conditions are closer to the Widom line. Although the differences in $\mathcal{P}(\xi)$ at $x/D \approx 5$ and 8, influenced by the potential core length, are similar to those in figures 21 and 30(*a*), significant differences are observed between the downstream $\mathcal{P}(\xi)$ profiles (at $x/D \approx 15$, 20 and 30) of case 4/4T in figure 30(*b*), unlike cases 2/2T. For case 4, the $\mathcal{P}(\xi)$ peaks are further away from the jet pure fluid concentration ($\xi = 1$) and are higher than in case 4T. The peaks in a symmetric unimodal p.d.f. coincide with the mean value, therefore, the differences in p.d.f. peak location and magnitude in figure 30(*b*) mirrors the differences observed in mean scalar values between case 4 and case 4T in figure 31(*a*).

4.4.2.5. Summary To summarize the above results, the variation of $p'_{c,rms}/p_c$ and $\rho'_{c,rms}/\rho_c$ with p_∞ and Z is similar for both inflows (containing different perturbations but same U_e), as shown in figures 27(*a*) and 27(*b*), and the variation can be estimated from the relative values of $p_\infty(\beta_T - 1/p_\infty)$ for various cases. However, $u'_{c,rms}/U_c$ shown in figure 24(*a*) varies differently for the two inflows. With decrease in Z, the proximity to the Widom line increases $u'_{c,rms}/U_c$ in the laminar-inflow jet, whereas the same decrease in Z has minimal influence on $u'_{c,rms}/U_c$ in pseudo-turbulent-inflow jet. This suggests that the real-gas effects, quantified by $p_\infty(\beta_T - 1/p_\infty)$, are strongly felt in the laminar inflow jets that contain large-scale coherent structures which generate regions of high mean strain rate, as shown in figure 32(*a*), whereas the same real-gas effects minimally influence

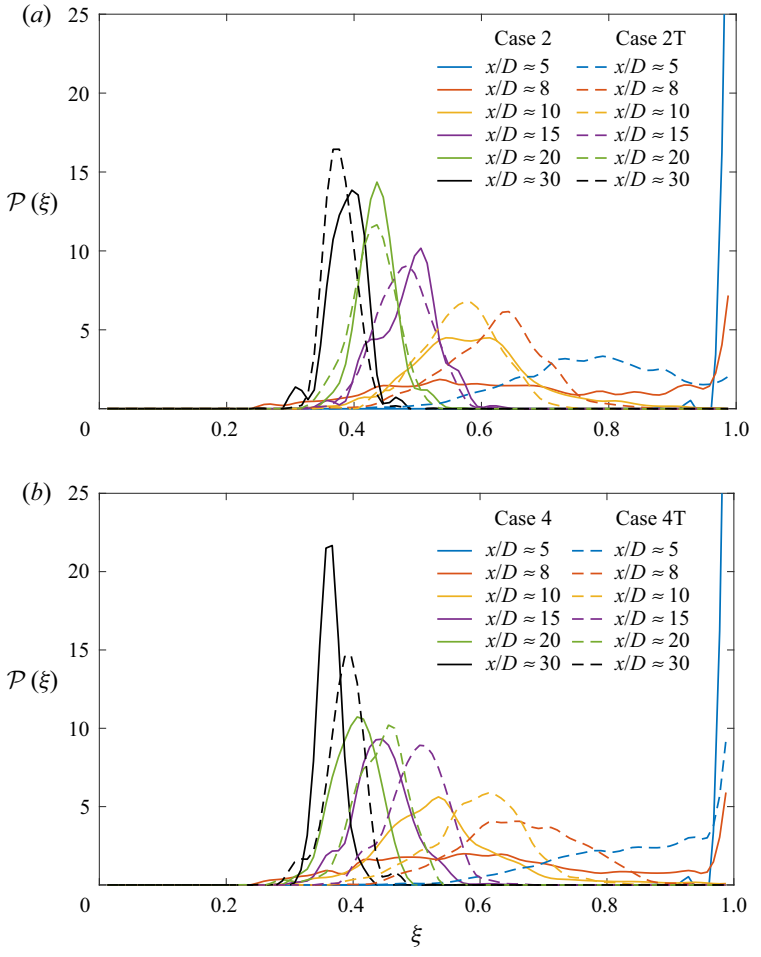

Figure 30. Scalar p.d.f., $\mathcal{P}(\xi)$, at various centreline axial locations for (*a*) cases 2 and 2T, and (*b*) cases 4 and 4T.

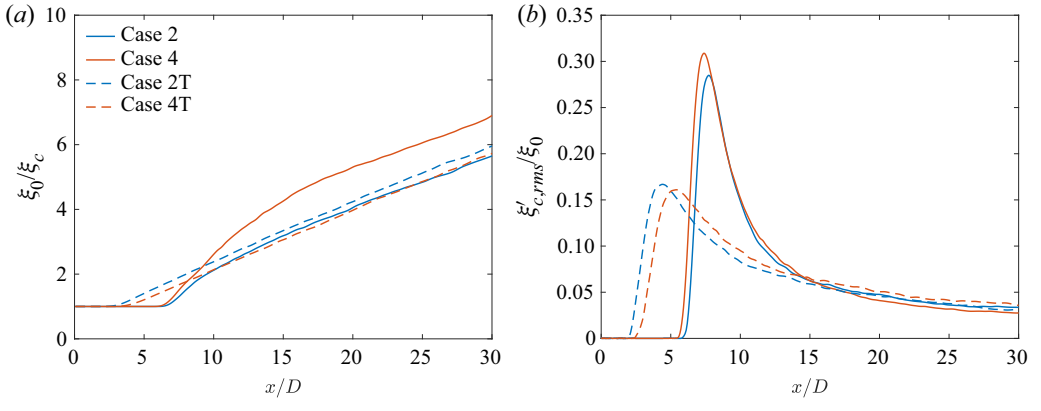

Figure 31. Streamwise variation of the (*a*) inverse of centreline scalar concentration (ξ_c) normalized by the jet-exit centreline value (ξ_0) and (*b*) centreline r.m.s. scalar fluctuation ($\xi'_{c,rms}$) normalized by the centreline jet-exit mean value (ξ_0).

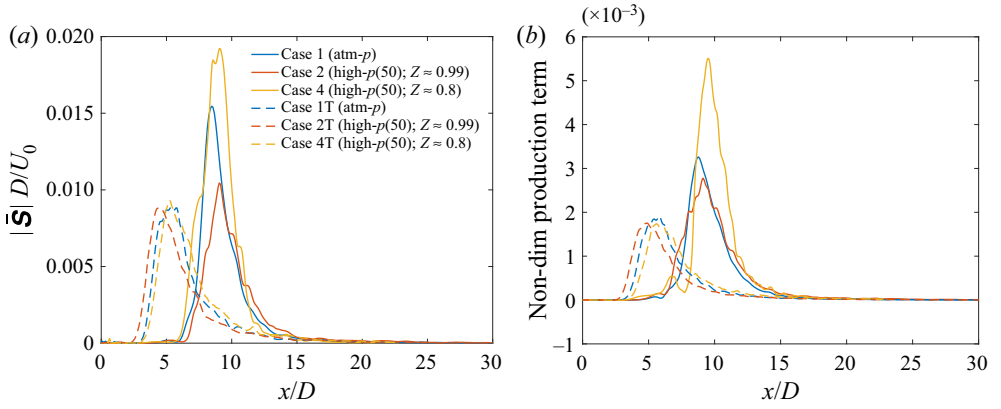

Figure 32. Centreline variation of (*a*) the strain rate magnitude, $|\bar{\boldsymbol{S}}| = (2\bar{S}_{ij}\bar{S}_{ij})^{1/2}$, normalized by U_0/D, where $\bar{S}_{ij}$ are the components of the mean rate-of-strain tensor, and (*b*) t.k.e. production term $P = -\bar{\rho}\widetilde{u_i''u_j''}(\partial\tilde{u}_i/\partial x_j)$ normalized by ρ_e (jet-exit density), U_0 and D, where tilde $(\tilde{\bullet})$ denotes the Favre average, $\tilde{\phi} = \overline{\rho\phi}/\bar{\rho}$, and $u_i'' = u_i - \tilde{u}_i$.

pseudo-turbulent-inflow jets. These results also showed that the effects of thermodynamic compressibility on the jet-flow dynamics cannot be directly determined from the variation of pressure fluctuations, instead fluctuating pressure–velocity correlation and third-order velocity moments (that determine t.k.e. diffusion fluxes from turbulent transport) are better correlated with the behaviour of the velocity field.

Studies of dynamic compressibility (e.g. Freund *et al.* 2000) divide compressibility modelling efforts into explicit and implicit approaches. An explicit approach targets modelling of the dilatational terms in the t.k.e. equation with the assumption that the turbulence characteristics are largely influenced by the compressible terms. In contrast, the implicit approaches assume that compressibility influences the structure of the turbulence, which in turn changes the turbulence energetics reflected in the t.k.e. production and turbulence transport terms. In this study, the behaviour of the t.k.e. production term, plotted in figure 32(*b*), and the turbulence transport terms, discussed above, follow the behaviour of $u'_{c,rms}/U_c$, which suggests that implicit modelling may be the physically correct approach for modelling of thermodynamic compressibility effects.

5. Conclusions

Turbulent round-jet DNS at perfect-gas (subcritical) and real-gas (supercritical) conditions were performed to compare and contrast the effects of thermodynamic and inflow condition on flow development and passive mixing. In all cases, the Reynolds number, Re_D, is 5000. The EOS and transport coefficient models were chosen to accurately represent the flow conditions. For supercritical pressures, the transport coefficient models were validated with the National Institute of Standards and Technology database. The thermodynamic conditions are characterized in terms of the ambient fluid compressibility factor, Z, and normalized isothermal compressibility, $p_\infty(\beta_T - 1/p_\infty)$. The inflow conditions are characterized in terms of the jet-exit bulk velocity (U_e) or Mach number (Ma_e) and the perturbation type, namely, a laminar inflow (with top-hat velocity profile and small random perturbations) or a pseudo-turbulent inflow (with statistics matching pipe-flow turbulence).

The first finding is that the mean axial velocity and Reynolds stress components attain self-similarity in high-p fully compressible jets, as they do in atmospheric-p jets. However, the self-similar profiles depend on the thermodynamic and inflow details, indicating that these details influence both the near- and far-field jet-flow dynamics. The transition region of the flow, immediately downstream of the potential core closure, exhibits greater sensitivity to those details than the self-similar region. Moreover, the laminar-inflow jets show larger differences with change in thermodynamic conditions than the pseudo-turbulent-inflow jets. The laminar inflow jets exhibit dominant coherent structures that generate a transition region with large mean strain rates, which enhance sensitivity to real-gas effects. These coherent structures also enhance the jet spread in laminar-inflow cases compared with pseudo-turbulent-inflow cases, where the jet spreads by entrainment through small-scale turbulence.

The second important finding is that the ambient thermodynamic conditions influence flow behaviour by modifying the structure of turbulence through t.k.e. production and transport. In jets with a fixed U_e and inflow perturbation, the normalized pressure/density fluctuations vary according to the value of $p_\infty(\beta_T - 1/p_\infty)$. Increasing $p_\infty(\beta_T - 1/p_\infty)$ enhances the normalized pressure/density fluctuations in both the laminar inflow and the pseudo-turbulent-inflow jets. However, the effect on velocity/scalar fluctuations depends on the extent of thermodynamic departure from perfect gas as well as the inflow perturbations. Large deviation of Z from unity and of $p_\infty(\beta_T - 1/p_\infty)$ from zero with laminar inflow triggers large normalized velocity/scalar fluctuations resulting in greater mixing. However, a small departure from perfect gas does not change the flow behaviour significantly. Moreover, the effect of thermodynamic changes on velocity/scalar statistics in pseudo-turbulent-inflow jets is small, despite significant variations in their pressure/density statistics. Velocity/scalar fluctuations that determine flow entrainment and mixing are not directly correlated with pressure fluctuations, but rather with the fluctuating pressure–velocity correlation that determines the turbulent transport in the t.k.e. equation due to pressure fluctuations. These results show that the thermodynamic condition, expressed in terms of Z or $p_\infty(\beta_T - 1/p_\infty)$, is insufficient to completely determine the flow behaviour that also depends on the inflow details. Thus, neither Z nor $p_\infty(\beta_T - 1/p_\infty)$ are self-similarity parameters.

The third important finding is that at large departures from perfect gas, U_e (from which the Mach number Ma_e is calculated that determines the dynamic compressibility) can strongly influence the flow dynamics and mixing. The ambient speed of sound differs according to the thermodynamic condition and, hence, a fixed U_e leads to different Ma_e across various flow cases. Variation of Ma_e over a small subsonic range shows that an increase in Ma_e with laminar inflow enhances velocity/scalar fluctuations leading to greater mixing. Variation of thermodynamic condition at a fixed Ma_e shows that the pressure/density fluctuations differ according to the value of Z; smaller Z leads to larger fluctuations. The velocity/scalar flucutations in high-p cases also vary according to the Z value. A detailed study of the effects of Ma_e is beyond the scope of this study and will be a subject of future investigation.

The jet-flow regions and metrics sensitive to p_∞, Z and inflow condition, identified in this study, may guide high-p experimental studies in obtaining measurements that may serve as databases for simulation and model validation. For example, the transition region of laminar-inflow jets exhibits high sensitivity to Z, and thus high-resolution measurements in that region may help in evaluating high-p model robustness and accuracy. The results from this study also demonstrate that high-p jet experiments performed at a fixed Z cannot be used to infer results for jets at same Z but larger p_∞. Moreover, the larger velocity/scalar

fluctuations when the Widom line is approached in laminar-inflow jets suggest that fuel–oxidizer mixing can be enhanced by combustor thermodynamic conditions closer to the Widom line with laminar fuel injection. Similarly, the correlation between the normalized pressure/density fluctuations and $p_\infty(\beta_T - 1/p_\infty)$ could be used to predict the thermodynamic fluctuations in a flow at real-gas thermodynamic conditions, without performing the flow simulations.

Funding. This work was supported at the California Institute of Technology by the Army Research Office under the direction of Dr R. Anthenien under grant number W911NF-16-1-0073. The computational resources were provided by the NASA Advanced Supercomputing Division at Ames Research Center under the T^3 program directed by Dr M. Rogers.

Declaration of interests. The authors report no conflict of interest.

Author ORCIDs.
Nek Sharan https://orcid.org/0000-0002-7274-8232;
Josette Bellan https://orcid.org/0000-0001-9218-7017.

Appendix A. Validation of the EOS and transport properties for high-p simulations

To examine the robustness of the PR EOS and transport coefficient models at supercritical conditions, figure 33 illustrates the density, isobaric heat capacity and the transport coefficients μ_{ph} and λ_{ph} calculated from the models described in § 2.3. The calculated values are compared against the National Institute of Standards and Technology (NIST) database (Lemmon *et al.* 2010) for N_2 at $p = 50$ and 70 bar in the T range 100–400 K, which includes the critical temperature T_{cr} =126.2 K of N_2. As evident, the models show good agreement with the NIST database, showing their validity at high-p conditions. The transport coefficient models are accurate only for $T > T_{cr}$ and, thus, the comparison of μ_{ph} and λ_{ph} only spans this range.

Appendix B. Grid convergence

An estimate of the Kolmogorov length scale in terms of Re_D, which may help determine the optimal grid spacing for DNS, can be made for incompressible (or weakly compressible) jet flows (Sharan & Bellan 2019). However, the estimates for incompressible flows may not necessarily apply in high-pressure regimes of interest here. Therefore, to ensure grid convergence, mean-flow statistics are compared in this section by successively refining the grid for cases 1 to 5 (see table 2), which ensures sufficient grid resolution for DNS.

Figure 34(*a–e*) compares the time-averaged centreline velocity, U_c, and scalar concentration, ξ_c, normalized by the jet-exit values U_0 and ξ_0 as a function of axial distance from simulations of cases 1 to 5 with various grid resolutions. Statistics for case 1 at atmospheric conditions converge at a resolution of $320 \times 288 \times 288$, whereas, for high-pressure cases, they converge around $400 \times 320 \times 320$, except case 4 at $Z = 0.8$ having maximum deviation from perfect gas among all cases considered that shows convergence around $480 \times 360 \times 360$. The plots also show that, in all cases, the scalar concentration begins to decay upstream of the velocity and at a faster rate than the velocity, consistent with the observation of (Lubbers *et al.* 2001, see figure 6) for a passive scalar diffusing at unity Schmidt number.

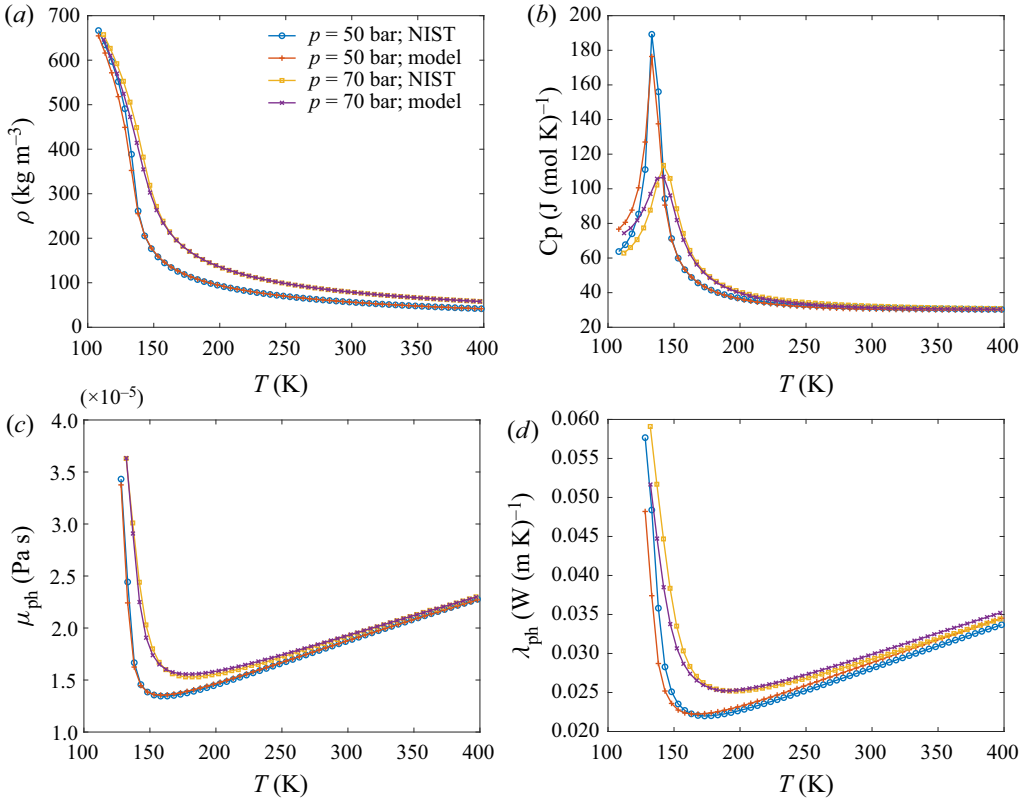

Figure 33. EOS and transport coefficient model comparison against NIST database for pure nitrogen at 50 bar pressure. (*a*) Density, (*b*) isobaric heat capacity, (*c*) viscosity and (*d*) thermal conductivity.

Appendix C. Validation of perfect-gas simulation: case 1 results

Quantitative experimental data for supercritical jets are rare, however, numerous measurements of high-order statistics have been made for jets at atmospheric conditions. For comparisons, the experimental measurements made in the self-similar region of density-matched jets, where the jet/chamber density ratio is approximately unity, are considered here, e.g. the velocity measurements of Wygnanski & Fiedler (1969), Panchapakesan & Lumley (1993) and Hussein *et al.* (1994), and the passive scalar measurements of Ebrahimi & Kleine (1977), Dowling & Dimotakis (1990) and Mi *et al.* (2001).

Figure 35 shows the decay of the time-averaged centreline velocity, $U_c(x)$, and centreline scalar concentration, $\xi_c(x)$, normalized by the jet-exit centreline velocity, U_0 $(= U_c(0))$, and scalar concentration, ξ_0 $(= \xi_c(0))$, respectively, for case 1. In the self-similar region, U_c varies with the reciprocal of the downstream distance, given by (e.g. Hussein *et al.* 1994)

$$\frac{U_c\,(x)}{U_0} = B_u\left(\frac{D}{x - x_{0u}}\right), \tag{C1}$$

where B_u is a constant and x_{0u} denotes the virtual origin derived from the centreline axial velocity. Similarly, the time-averaged centreline scalar concentration has

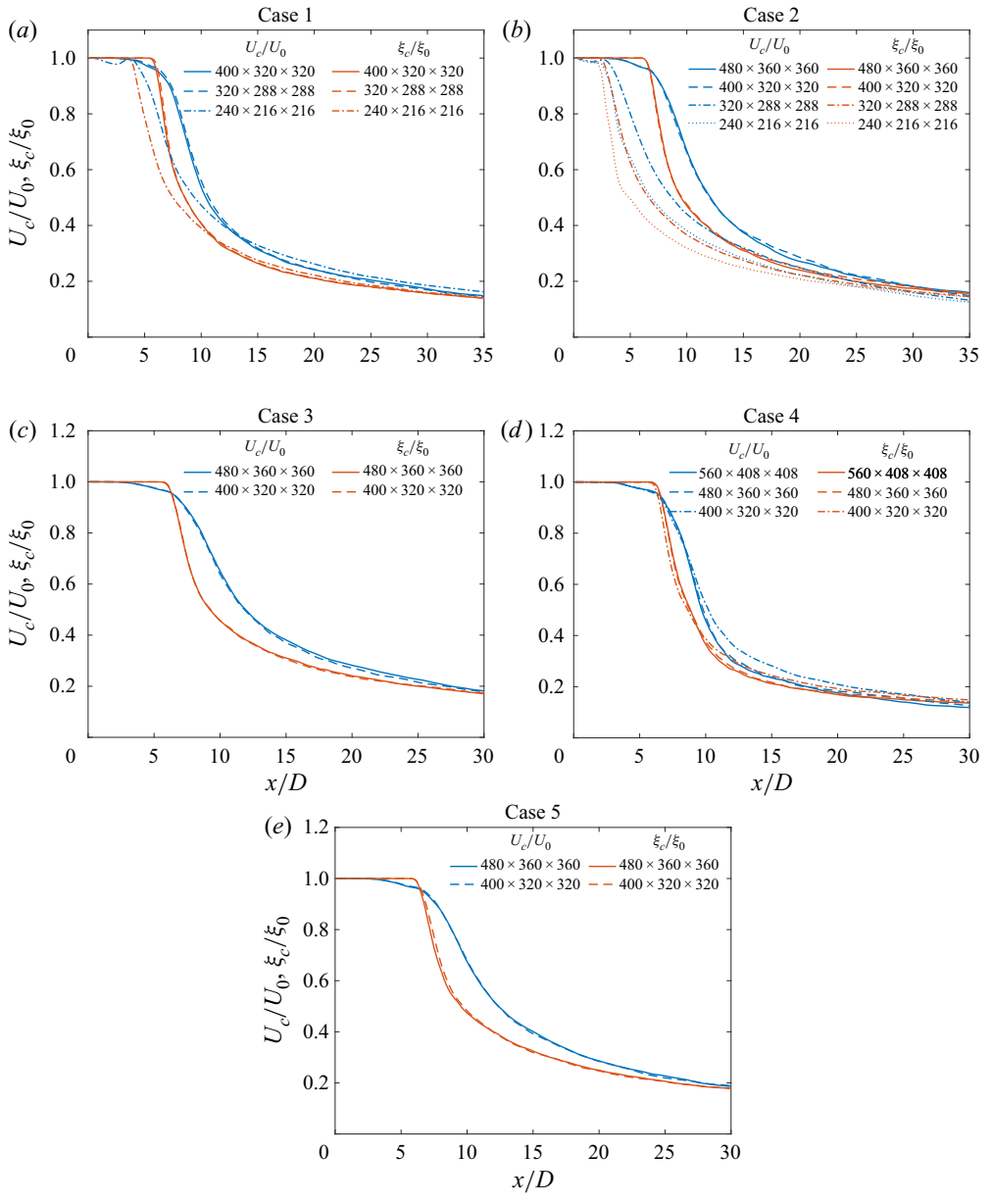

Figure 34. Time-averaged centreline velocity (U_c) and scalar (ξ_c) values normalized by the jet-exit values U_0 and ξ_0 as a function of axial distance for various grid resolutions. (*a*) case 1, (*b*) case 2, (*c*) case 3, (*d*) case 4 and (*e*) case 5.

the form

$$\frac{\xi_c\,(x)}{\xi_0} = B_\xi \left(\frac{D}{x - x_{0\xi}}\right), \tag{C2}$$

where B_ξ is a constant and $x_{0\xi}$ denotes the virtual origin derived from the centreline scalar variation. Simultaneous measurements of the velocity and scalar field in a single experiment were not found in the literature and, therefore, data from different studies

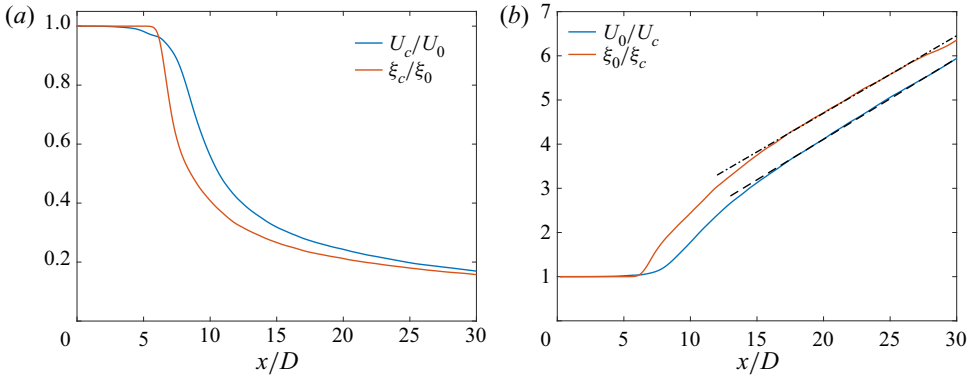

Figure 35. Case 1 results: streamwise variation of the (a) centreline mean velocity (U_c) and scalar concentration (ξ_c) normalized by the respective jet-exit centreline mean values, U_0 and ξ_0, as a function of axial distance and (b) inverse of the normalized time-averaged centreline values showing linear decay asymptotically with axial distance. The dashed line uses $B_u = 5.5$, $x_{0u} = -2.4D$ in (C1) and the dash-dotted line uses $B_\xi = 5.7$, $x_{0\xi} = -6.8D$ in (C2).

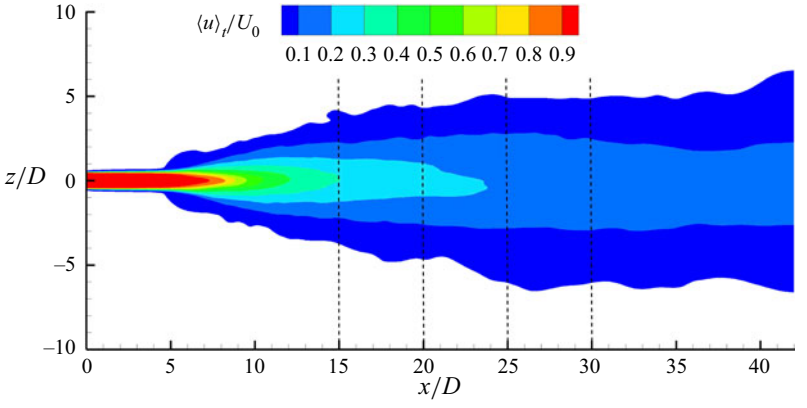

Figure 36. Time-averaged axial-velocity contours for case 1. The dashed lines show axial locations where statistics are azimuthally averaged.

are used for comparing the velocity and scalar fields. The dashed and dash-dotted lines in figure 35(b) show the profiles for $B_u = 5.5$ and $B_\xi = 5.7$, respectively. They are comparable to the experimentally observed values of $B_u = 5.7$, 6.06 and 5.8 by Wygnanski & Fiedler (1969), Panchapakesan & Lumley (1993) and Hussein *et al.* (1994), respectively, and of $B_\xi = 5.78$ and 5.11 by Ebrahimi & Kleine (1977) and Dowling & Dimotakis (1990), respectively.

Contours of $\langle u\rangle_t/U_0$ in the $y/D = 0$ plane are depicted in figure 36, with dashed lines showing the axial locations where $\bar{u}/U_c$ and $\bar{\xi}/\xi_c$ are plotted in figures 37(a) and 37(b), respectively. The azimuthal averages for calculations of $\bar{u}$ and $\bar{\xi}$ using (3.3) are performed by interpolation of the time-averaged Cartesian-grid solution to a polar grid at respective axial locations. The variation of $\bar{u}/U_c$ with the similarity coordinate, $\eta = r/(x - x_{0u})$, is compared with the self-similar profile from experiments in figure 37(a). The simulation results at various axial locations agree well with each other and with the experimental profiles, indicating that the mean axial velocity becomes self-similar around $x/D \approx 15$ for this case. Values of $\bar{\xi}/\xi_c$ at various x/D locations are compared against the self-similar

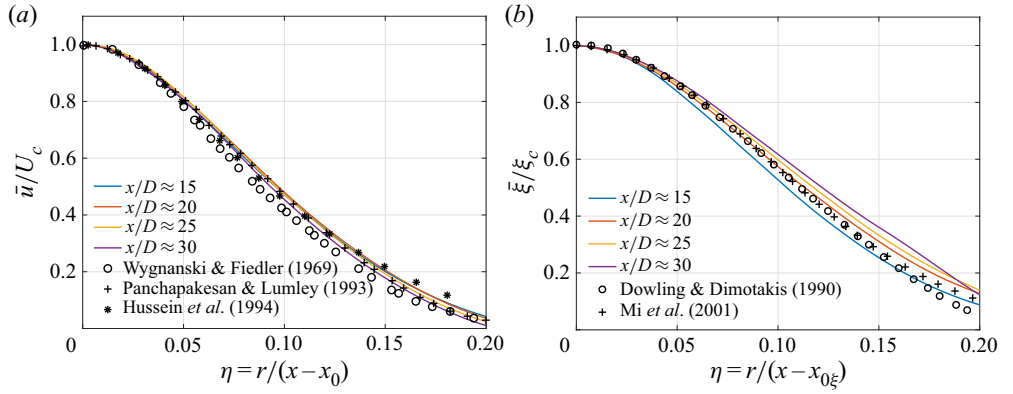

Figure 37. Case 1 results. (*a*) Mean axial velocity ($\bar{u}$) normalized by the centreline mean velocity (U_c) and (*b*) mean scalar concentration ($\tilde{\xi}$) normalized by the centreline mean scalar value at various axial locations plotted as a function of similarity coordinates. The velocity profiles are compared against the self-similar profiles from the experiments of Wygnanski & Fiedler (1969), Panchapakesan & Lumley (1993) and Hussein *et al.* (1994), whereas the scalar profiles are compared against the experimental profiles of Dowling & Dimotakis (1990) and Mi *et al.* (2001).

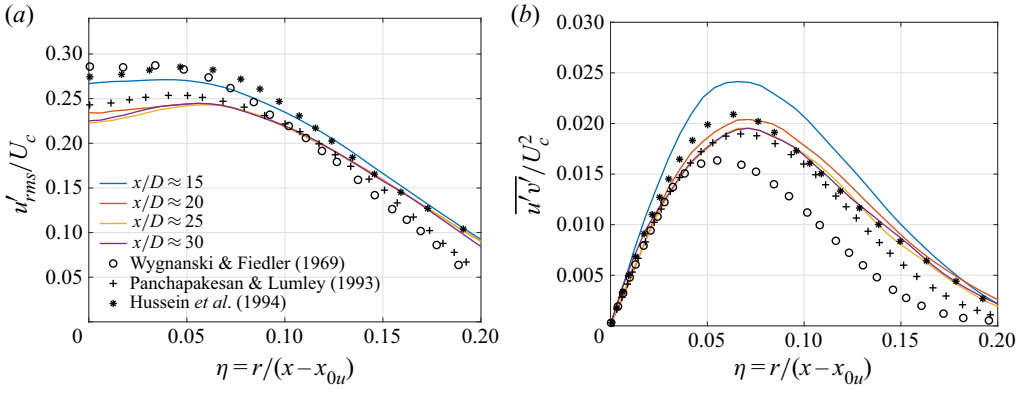

Figure 38. Case 1 results. (*a*) The r.m.s. axial-velocity fluctuations (u'_{rms}), and (*b*) Reynolds stress ($\overline{u'v'}$) normalized by the centreline mean velocity at various axial locations plotted as a function of similarity coordinates compared against the self-similar profiles from the experiments of Wygnanski & Fiedler (1969), Panchapakesan & Lumley (1993) and Hussein *et al.* (1994). The legend is the same for both plots.

profiles of Dowling & Dimotakis (1990) and Mi *et al.* (2001) in figure 37(*b*). As evident from the figure, there are minor differences between the profiles at various axial locations, suggesting that the mean scalar concentration is not fully self-similar, but close to self-similarity around $x/D \approx 30$.

To further examine the velocity field, figure 38(*a*,*b*) show the radial variation of normalized r.m.s. axial-velocity fluctuation and Reynolds stress compared against the self-similar profile from experiments. The simulation profiles at $x/D \approx 25$ and $x/D \approx 30$, in figure 38, agree well with each other, indicating that these quantities attain self-similarity downstream of $x/D \approx 20$. The simulation self-similar profiles also lie within the experimentally observed self-similar profiles of these quantities.

The favourable comparisons between simulation results and experimental measurements indicate that the governing equations with perturbed laminar inflow and the numerical

method accurately simulate the jet exiting a smooth contracting nozzle at atmospheric-p. More comparisons are not included here for brevity, but can be found in Sharan & Bellan (2021).

References

Baab, S., Förster, F.J., Lamanna, G. & Weigand, B. 2016 Speed of sound measurements and mixing characterization of underexpanded fuel jets with supercritical reservoir condition using laser-induced thermal acoustics. *Exp. Fluids* **57** (11), 1–13.

Baab, S., Steinhausen, C., Lamanna, G., Weigand, B. & Förster, F.J. 2018 A quantitative speed of sound database for multi-component jet mixing at high pressure. *Fuel* **233**, 918–925.

Balaras, E., Piomelli, U. & Wallace, J.M. 2001 Self-similar states in turbulent mixing layers. *J. Fluid Mech.* **446**, 1–24.

Banuti, D.T., Raju, M. & Ihme, M. 2017 Similarity law for Widom lines and coexistence lines. *Phys. Rev.* E **95** (5), 052120.

Bodony, D.J. 2006 Analysis of sponge zones for computational fluid mechanics. *J. Comput. Phys.* **212** (2), 681–702.

Boersma, B.J., Brethouwer, G. & Nieuwstadt, F. 1998 A numerical investigation on the effect of the inflow conditions on the self-similar region of a round jet. *Phys. Fluids* **10** (4), 899–909.

Chehroudi, B., Talley, D. & Coy, E. 2002 Visual characteristics and initial growth rates of round cryogenic jets at subcritical and supercritical pressures. *Phys. Fluids* **14** (2), 850–861.

Dowling, D.R. & Dimotakis, P.E. 1990 Similarity of the concentration field of gas-phase turbulent jets. *J. Fluid Mech.* **218**, 109–141.

Ebrahimi, I. & Kleine, R. 1977 Konzentrationsfelder in isothermen luft-freistrahlen. *Forsch. Ingen.* A **43** (1), 25–30.

Eggels, J., Unger, F., Weiss, M.H., Westerweel, J., Adrian, R.J., Friedrich, R. & Nieuwstadt, F. 1994 Fully developed turbulent pipe flow: a comparison between direct numerical simulation and experiment. *J. Fluid Mech.* **268**, 175–210.

Falgout, Z., Rahm, M., Wang, Z. & Linne, M. 2015 Evidence for supercritical mixing layers in the ECN Spray A. *Proc. Combust. Inst.* **35** (2), 1579–1586.

Freund, J.B., Lele, S.K. & Moin, P. 2000 Compressibility effects in a turbulent annular mixing layer. Part 1. Turbulence and growth rate. *J. Fluid Mech.* **421**, 229–267.

Gao, W., Lin, Y., Hui, X., Zhang, C. & Xu, Q. 2019 Injection characteristics of near critical and supercritical kerosene into quiescent atmospheric environment. *Fuel* **235**, 775–781.

George, W.K. 1989 The self-preservation of turbulent flows and its relation to initial conditions and coherent structures. In *Advances in Turbulence* (ed. R. Arndt & W.K. George), pp. 39–73. Hemisphere.

George, W.K. & Davidson, L. 2004 Role of initial conditions in establishing asymptotic flow behavior. *AIAA J.* **42** (3), 438–446.

Ghosal, S. & Rogers, M.M. 1997 A numerical study of self-similarity in a turbulent plane wake using large-eddy simulation. *Phys. Fluids* **9** (6), 1729–1739.

Gnanaskandan, A. & Bellan, J. 2017 Numerical simulation of jet injection and species mixing under high-pressure conditions. *J. Phys.* **821**, 012020.

Gnanaskandan, A. & Bellan, J. 2018 Side-jet effects in high-pressure turbulent flows: direct numerical simulation of nitrogen injected into carbon dioxide. *J. Supercrit. Fluids* **140**, 165–181.

Grinstein, F.F. 2001 Vortex dynamics and entrainment in rectangular free jets. *J. Fluid Mech.* **437**, 69–101.

Harstad, K.G., Miller, R.S. & Bellan, J. 1997 Efficient high-pressure state equations. *AIChE J.* **43** (6), 1605–1610.

Ho, C.M. & Nosseir, N.S. 1981 Dynamics of an impinging jet. Part 1. The feedback phenomenon. *J. Fluid Mech.* **105**, 119–142.

Husain, Z.D. & Hussain, A.K.M.F. 1979 Axisymmetric mixing layer: influence of the initial and boundary conditions. *AIAA J.* **17** (1), 48–55.

Hussein, H.J., Capp, S.P. & George, W.K. 1994 Velocity measurements in a high-Reynolds-number, momentum-conserving, axisymmetric, turbulent jet. *J. Fluid Mech.* **258**, 31–75.

Kennedy, C.A. & Carpenter, M.H. 1994 Several new numerical methods for compressible shear-layer simulations. *Appl. Numer. Maths* **14** (4), 397–433.

Klein, M., Sadiki, A. & Janicka, J. 2003 A digital filter based generation of inflow data for spatially developing direct numerical or large eddy simulations. *J. Comput. Phys.* **186** (2), 652–665.

Lele, S.K. 1994 Compressibility effects on turbulence. *Annu. Rev. Fluid Mech.* **26** (1), 211–254.

LEMMON, E.W., *et al.* 2010 NIST standard reference database 23. NIST Reference Fluid Thermodynamic and Transport Properties – REFPROP, Version 9, 55.

LODATO, G., DOMINGO, P. & VERVISCH, L. 2008 Three-dimensional boundary conditions for direct and large-eddy simulation of compressible viscous flows. *J. Comput. Phys.* **227** (10), 5105–5143.

LUBBERS, C.L., BRETHOUWER, G. & BOERSMA, B.J. 2001 Simulation of the mixing of a passive scalar in a round turbulent jet. *Fluid Dyn. Res.* **28** (3), 189–208.

LUND, T.S., WU, X. & SQUIRES, K.D. 1998 Generation of turbulent inflow data for spatially-developing boundary layer simulations. *J. Comput. Phys.* **140** (2), 233–258.

MASI, E., BELLAN, J., HARSTAD, K.G. & OKONG'O, N.A. 2013 Multi-species turbulent mixing under supercritical-pressure conditions: modelling, direct numerical simulation and analysis revealing species spinodal decomposition. *J. Fluid Mech.* **721**, 578–626.

MATTNER, T.W. 2011 Large-eddy simulations of turbulent mixing layers using the stretched-vortex model. *J. Fluid Mech.* **671**, 507–534.

MAYER, W., SCHIK, A., AXEL, H., VIELLE, B., CHAUVEAU, C., G-OKALP, I., TALLEY, D.G. & WOODWARD, R.D. 1998 Atomization and breakup of cryogenic propellants under high-pressure subcritical and supercritical conditions. *J. Propul. Power* **14** (5), 835–842.

MAYER, W., TELAAR, J., BRANAM, R., SCHNEIDER, G. & HUSSONG, J. 2003 Raman measurements of cryogenic injection at supercritical pressure. *Heat Mass Transfer* **39** (8–9), 709–719.

MI, J., NOBES, D.S. & NATHAN, G.J. 2001 Influence of jet exit conditions on the passive scalar field of an axisymmetric free jet. *J. Fluid Mech.* **432**, 91–125.

MICHALKE, A. 1984 Survey on jet instability theory. *Prog. Aerosp. Sci.* **21**, 159–199.

MORRIS, P.J. 1983 Viscous stability of compressible axisymmetric jets. *AIAA J.* **21** (4), 481–482.

MUTHUKUMARAN, C.K. & VAIDYANATHAN, A. 2016*a* Initial instability of round liquid jet at subcritical and supercritical environments. *Phys. Fluids* **28** (7), 074104.

MUTHUKUMARAN, C.K. & VAIDYANATHAN, A. 2016*b* Mixing nature of supercritical jet in subcritical and supercritical conditions. *J. Propul. Power* **33** (4), 842–857.

NEWMAN, J.A. & BRZUSTOWSKI, T.A. 1971 Behavior of a liquid jet near the thermodynamic critical region. *AIAA J.* **9** (8), 1595–1602.

OKONG'O, N. & BELLAN, J. 2002*a* Consistent boundary conditions for multicomponent real gas mixtures based on characteristic waves. *J. Comput. Phys.* **176** (2), 330–344.

OKONG'O, N.A. & BELLAN, J. 2002*b* Direct numerical simulation of a transitional supercritical binary mixing layer: heptane and nitrogen. *J. Fluid Mech.* **464**, 1–34.

OKONG'O, N.A., HARSTAD, K. & BELLAN, J. 2002 Direct numerical simulations of O_2/H_2 temporal mixing layers under supercritical conditions. *AIAA J.* **40** (5), 914–926.

OSCHWALD, M. & SCHIK, A. 1999 Supercritical nitrogen free jet investigated by spontaneous raman scattering. *Exp. Fluids* **27** (6), 497–506.

PANCHAPAKESAN, N.R. & LUMLEY, J.L. 1993 Turbulence measurements in axisymmetric jets of air and helium. Part 1. Air jet. *J. Fluid Mech.* **246**, 197–223.

PANTANO, C. & SARKAR, S. 2002 A study of compressibility effects in the high-speed turbulent shear layer using direct simulation. *J. Fluid Mech.* **451**, 329–371.

PAPAMOSCHOU, D. & ROSHKO, A. 1988 The compressible turbulent shear layer: an experimental study. *J. Fluid Mech.* **197**, 453–477.

POINSOT, T.J. & LELE, S.K. 1992 Boundary conditions for direct simulations of compressible viscous flows. *J. Comput. Phys.* **101** (1), 104–129.

POLING, B.E., *et al.* 2001 *The Properties of Gases and Liquids*, vol. 5. McGraw-Hill.

POURSADEGH, F., LACEY, J.S., BREAR, M.J. & GORDON, R.L. 2017 On the fuel spray transition to dense fluid mixing at reciprocating engine conditions. *Energy Fuels* **31** (6), 6445–6454.

RICHARDS, C.D. & PITTS, W.M. 1993 Global density effects on the self-preservation behaviour of turbulent free jets. *J. Fluid Mech.* **254**, 417–435.

RIES, F., OBANDO, P., SHEVCHUCK, I., JANICKA, J. & SADIKI, A. 2017 Numerical analysis of turbulent flow dynamics and heat transport in a round jet at supercritical conditions. *Intl J. Heat Fluid Flow* **66**, 172–184.

ROY, A., JOLY, C. & SEGAL, C. 2013 Disintegrating supercritical jets in a subcritical environment. *J. Fluid Mech.* **717**, 193–202.

SCHMITT, T., SELLE, L., RUIZ, A. & CUENOT, B. 2010 Large-eddy simulation of supercritical-pressure round jets. *AIAA J.* **48** (9), 2133–2144.

SCIACOVELLI, L. & BELLAN, J. 2019 The influence of the chemical composition representation according to the number of species during mixing in high-pressure turbulent flows. *J. Fluid Mech.* **863**, 293–340.

SEGAL, C. & POLIKHOV, S.A. 2008 Subcritical to supercritical mixing. *Phys. Fluids* **20** (5), 052101.

SELLE, L. & SCHMITT, T. 2010 Large-eddy simulation of single-species flows under supercritical thermodynamic conditions. *Combust. Sci. Technol.* **182** (4–6), 392–404.

SHARAN, N. 2016 Time-stable high-order finite difference methods for overset grids. PhD thesis, University of Illinois at Urbana-Champaign.

SHARAN, N. & BELLAN, J.R. 2019 Numerical aspects for physically accurate direct numerical simulations of turbulent jets. *AIAA Paper* 2019-2011.

SHARAN, N. & BELLAN, J.R. 2021 Direct numerical simulation of high-pressure free jets. *AIAA Paper* 2021-0550.

SHARAN, N., MATHEOU, G. & DIMOTAKIS, P.E. 2018*a* Mixing, scalar boundedness, and numerical dissipation in large-eddy simulations. *J. Comput. Phys.* **369**, 148–172.

SHARAN, N., MATHEOU, G. & DIMOTAKIS, P.E. 2019 Turbulent shear-layer mixing: initial conditions, and direct-numerical and large-eddy simulations. *J. Fluid Mech.* **877**, 35–81.

SHARAN, N., PANTANO, C. & BODONY, D.J. 2018*b* Time-stable overset grid method for hyperbolic problems using summation-by-parts operators. *J. Comput. Phys.* **361**, 199–230.

SIMEONI, G.G., BRYK, T., GORELLI, F.A., KRISCH, M., RUOCCO, G., SANTORO, M. & SCOPIGNO, T. 2010 The widom line as the crossover between liquid-like and gas-like behaviour in supercritical fluids. *Nat. Phys.* **6** (7), 503–507.

SIMONE, A., COLEMAN, G.N. & CAMBON, C. 1997 The effect of compressibility on turbulent shear flow: a rapid-distortion-theory and direct-numerical-simulation study. *J. Fluid Mech.* **330**, 307–338.

SLESSOR, M.D., BOND, C.L. & DIMOTAKIS, P.E. 1998 Turbulent shear-layer mixing at high Reynolds numbers: effects of inflow conditions. *J. Fluid Mech.* **376**, 115–138.

TAŞKINOĞLU, E.S. & BELLAN, J. 2010 A posteriori study using a DNS database describing fluid disintegration and binary-species mixing under supercritical pressure: heptane and nitrogen. *J. Fluid Mech.* **645**, 211–254.

TAŞKINOĞLU, E.S. & BELLAN, J. 2011 Subgrid-scale models and large-eddy simulation of oxygen stream disintegration and mixing with a hydrogen or helium stream at supercritical pressure. *J. Fluid Mech.* **679**, 156–193.

TOWNSEND, A. 1980 *The Structure of Turbulent Shear Flow*. Cambridge University Press.

VREMAN, A.W., SANDHAM, N.D. & LUO, K.H. 1996 Compressible mixing layer growth rate and turbulence characteristics. *J. Fluid Mech.* **320**, 235–258.

WOODWARD, R. & TALLEY, D. 1996 Raman imaging of transcritical cryogenic propellants. *AIAA Paper* 1996-468.

WYGNANSKI, I., CHAMPAGNE, F. & MARASLI, B. 1986 On the large-scale structures in two-dimensional, small-deficit, turbulent wakes. *J. Fluid Mech.* **168**, 31–71.

WYGNANSKI, I. & FIEDLER, H.O. 1969 Some measurements in the self-preserving jet. *J. Fluid Mech.* **38** (3), 577–612.

XU, G. & ANTONIA, R. 2002 Effect of different initial conditions on a turbulent round free jet. *Exp. Fluids* **33** (5), 677–683.